

The central bar in M 94

C. Möllenhoff¹ *, M. Matthias^{1,2}, and O. E. Gerhard^{1,2}

¹ Landessternwarte, Königstuhl 12, D-69117 Heidelberg, Germany
e-mail: cmoellen@mail.lsw.uni-heidelberg.de

² Astronomisches Institut, Universität Basel, Venusstr. 7, CH-4102 Binningen, Switzerland
e-mail: matthias@astro.unibas.ch, gerhard@astro.unibas.ch

Received Aug. 1994; accepted

Abstract. Visual, NIR, and H_α surface photometry of the oval disk galaxy M 94 (NGC 4736) was performed to study the distribution of mass in old stars and the distribution of the warm emission line gas. The radial profile of the inner stellar disk is steeper than exponential and displays twisted and deformed isophotes. Dust is not responsible for these deviations. The investigation of a number of morphological models showed that M 94 has a weak central stellar bar of 0.7 kpc major axis length which comprises about 14% of the total light within $20''$.

By means of longslit spectroscopy the kinematics of gas and stars in this region were investigated. The stellar kinematics reveal the existence of a small spheroidal bulge with $v/\sigma \approx 0.8$. The stellar velocity field in this region is approximately axisymmetric, showing that the effects of the bar on the kinematics of the hot component are relatively small. The warm gas in the bar region shows global and local deviations from the stellar kinematics, but outside the central bar fits into the general HI velocity field.

Model calculations of closed orbits for gas in the potential of the bar perturbation and axisymmetric disk and bulge predict large non-circular motions for cold gas in equilibrium flow. These do not fit the central H_α kinematics; rather it appears that the H_α gas must have large random motions and is not in a steady state, and that hydrodynamical effects due to a recent starburst play a role in the central region.

Key words:

1. Introduction

M 94 = NGC 4736 is an Sab spiral galaxy at a distance of ≈ 6.6 Mpc. It is well studied in optical morphology, optical emission gas kinematics (van der Kruit 1974, 1976, Buta 1984, 1988) and HI distribution and kinematics (Bosma et al 1977, Mulder & van Driel 1993). There exist several good overviews about these results and other characteristics of M 94 in the literature (e.g. Buta 1984, Mulder & van Driel 1993). Since this paper deals mainly with new optical and NIR results (morphology, stellar kinematics, gas kinematics) we present here only a brief summary of the most important optical features of this galaxy. Basic parameters of M 94 and the most numerical results from this study are presented in Table 1.

Bosma et al (1977) distinguished the following five annular zones with progressively lower surface brightness in M 94:

1. A bright central region (bulge), $R < 15''$.
2. A zone of inner spiral structure $R \approx 15$ to $50''$. This zone is bounded by a bright inner ring.
3. A zone of outer spiral structure, $R \approx 50$ to $\approx 200''$, this region probably forms an oval disk.
4. A zone of low surface brightness (*gap*).
5. A faint outer ring of $R \approx 330''$.

The nuclear region is extremely bright; according to Keel and Weedman (1978) M 94 is one of the galaxies with the highest optical surface brightness. The inner ring of radius $\approx 40''$ to $50''$, shows HII regions and young blue objects, characteristic for strong star formation. The interpretation of this ring is the subject of numerous papers. In a detailed study of the kinematics van der Kruit (1974, 1976) attempted to fit a variety of kinematical models to the ring. He concluded that the velocity field is best interpreted in terms of a uniform radial expansion from the nucleus. However, using Fabry-Perot data Buta (1984, 1988) concluded that the ring is better interpreted as the result of a secular evolution in this galaxy due to a Lindblad resonance.

Send offprint requests to: C. Möllenhoff

* Visiting astronomer of the German-Spanish Astronomical Center, Calar Alto, operated by the Max-Planck-Institut für Astronomie, Heidelberg jointly with the Spanish National Commission for Astronomy.

The bright inner ring was also observed in CO by Gerin et al (1991). They followed the formation of the outer and the inner ring in a model where the main disk of M 94 is a massive oval with $b/a = 0.8$. That the disk of M 94 is not axially symmetric had already been seen by Bosma et al (1977).

The zone inside the inner ring displays a strong isophote twist. This could be the consequence of a triaxial bulge (Beckman et al 1991) or a central secondary bar (Kormendy 1993). Such a 'bar within a bar' would rotate much faster than the large outer oval disk (Shlosman et al 1989, Friedli and Martinet 1993). A third interpretation was given by Shaw et al (1993), who proposed that this structure is the result of a combined stellar- and gas-dynamical mechanism. In the potential of the rotating oval disk a gas ring forms which perturbs the central stellar distribution. This perturbation is misaligned with respect to the outer oval disk but has the same angular speed; thus it is not an independent bar.

The aim of this paper is to study the distribution and kinematics of stars and gas in the central region of NGC 4736, and to compare these with model calculations. In Sect. 2 we describe the observations: (1) Surface photometry in the visual region (V, I, H_α) and in the NIR (J, K), in order to study the distribution the old stellar component as well as that of the dust and warm, line-emitting gas. (2) Longslit spectroscopy for the investigation of the kinematics of stars and gas in this region. The data reduction and the results are described In Sect. 3. In Sect. 4 we present morphological models for M 94. In Sect. 5 orbit families in a corresponding model potential are calculated and are used to model the kinematics of stars and gas. Their predictions will be compared with the observed kinematics. In Section 6 we discuss our results, and the conclusions of this paper are given in Section 7 .

2. Observations

2.1. CCD surface photometry

The CCD imaging observations were performed in February 1990, in January 1992, and in July 1993 at the German-Spanish Astronomical Center on Calar Alto, Spain. The Calar Alto 1.23m telescope was used in three different setup modi for CCD imaging: (1) The Landessternwarte focal reducer at the Cassegrain focus with a GEC P8603/A chip (576×386 pixels, 1 pix of $22\mu \hat{=} 1.56''$) and V, I filters; (2) the Calar Alto Cassegrain focus CCD camera with a coated GEC chip (576×386 pixels, 1 pix of $22\mu \hat{=} 0.46''$) and I filter; (3) the Cassegrain focus CCD camera with a Tektronix chip (512×512 pixels, 1 pix of $27\mu \hat{=} 0.56''$) and H_α filter. The exposure times were 1 minute (I filter) and 3 minutes (V) with the focal reducer, 15 minutes (I) and 45 minutes (H_α filter) with the Cassegrain camera. Photometric standard stars were

exposed several times during the night for the flux calibration. Flat field exposures were taken during evening and morning dusk; the telescope was slightly displaced between each exposure, to allow the elimination of stellar images in the flat field frames by an appropriate filtering procedure.

2.2. NIR surface photometry

The NIR imaging observations were performed in January 1994 with the 2.2m telescope of the German-Spanish Astronomical Center on Calar Alto, Spain. J, K images were obtained with the MPIA MAGIC camera (Herbst et al 1993). MAGIC has a 256×256 NICMOS3 HgCdTe detector array and was used in an imaging mode of $0.66''/\text{pix}$, corresponding to a field of $169'' \times 169''$. 3 exposures of 20 sec were added in the camera electronics, using a 'sample up the ramp' readout mechanism. Then the telescope was moved by a few arcsec for the next exposure, and another few arcsec for a third exposure, in order to get rid of the bad pixels. In total six such triples, i.e. 18 images of 1 min exposure time were obtained in each filter. Between the galaxy exposures the telescope was moved approx. half a degree offset for 3 blank sky images of the same expore times, also shifted slightly from each other to remove background stars. Photometric standard stars were exposed for the flux calibration, the sky exposures serve as flat fields.

2.3. Kinematics of the stars

The spectroscopic observations were done during February 1990 with the 2.2m telescope of the German-Spanish Astronomical Center on Calar Alto, Spain. Longslit spectrograms were obtained using the standard Boller & Chivens spectrograph in 4 slit orientations, $P.A. = 0^\circ, 45^\circ, 90^\circ, 135^\circ$ respectively. The detector was an RCA CCD with 1024×640 pixels of 15μ size. The slit width was 250μ or $2.9''$.

For the stellar kinematics we used a grid with 1200 lines/mm in the wavelength range $4500 - 5400 \text{ \AA}$ (resolution $0.9 \text{ \AA}/\text{pix}$). 3 pixels (or $2.7''$) along the slit were binned during readout. The exposure times were $2 \times 1h$ for each slit position.

Several stellar templates of spectral type between G8 III and K5 III were exposed for the subsequent Fourier-Cross-Correlation. The internal He-Ar lamp was used for wavelength calibration. A large number of domeflats with different exposure times were exposed for the correction of the nonlinear columns of the RCA chip at low light levels. Skyflats were obtained to correct for the profile along the slit.

2.4. Kinematics of the gas

The spectrograms for the kinematics of the emission gas of the HII regions were obtained during the same observing

run with the same slit width and orientations as above. The grid for the gas kinematics had 1200 lines/mm in the wavelength range 6200 – 7100 Å, and the exposure times here were 30 min for each spectrogram. The full spatial resolution of 0.9''/pix along the slit was used.

During a second spectroscopic run in January 1994 gas spectrograms in further slit orientations $P.A. = 28^\circ, 73^\circ, 118^\circ, 163^\circ$ respectively, were obtained with the same spectrograph and grating at the same telescope. However, this time a Tektronix chip 1024 x 1024 of 24μ pixelsize, slit width 370μ or $4.3''$, and spatial resolution of $1.47''$ /pix was used. The above given slit orientations correspond to the position angle of the central bar in M 94 (Sect. 3.1).

3. Data reduction and results

3.1. CCD surface photometry

The CCD images were reduced using the standard procedure with bias subtraction and flatfield division. An intensity-dependant median filter was applied which smoothed the images only in the outer zones of low S/N ratio but not in the central region of the galaxy.

Figure 1 shows the central 2×2 arcmin of the I image of M 94. The slightly irregular outer structure is the well known oval ring of HII regions, not very pronounced in this deep red image. While the major axes of the outer isophotes at $r \approx 40''$ have a position angle ($P.A.$) $\approx 120^\circ$, they are nearly circular at $r \approx 20''$. Further inside the position angle changes to $\approx 28^\circ$, and the isophotes display a distinctly *cusped* structure. Beckman et al (1991) interpreted the isophote twist as a signature for a triaxial bulge. However, the occurrence of cusped isophotes makes it more plausible that a bar-like structure of $\sim 30'' = 1.0$ kpc length is superposed onto the inner disk of M 94. This bar was already mentioned in Kormendy (1993).

A third interpretation was given by Shaw et al (1993), who proposed that this structure is the result of a combined stellar- and gas-dynamical mechanism: The oval disk leads to an accumulation of gas in a non-axisymmetric circumnuclear ring which becomes phase-shifted with respect to the original stellar oval disk. This ring has sufficient mass to induce a triaxial perturbation in the central stellar component. This perturbation is misaligned with respect to the outer oval disk but has the same angular speed; thus it is not an independent bar.

How does the isophote twist model of Shaw et al (1993) compare with our observations? Shaw et al give only rather general statements about the shape of the isophotes to be expected; it is difficult to make a comparison with the observed morphological details. They interpret the region of isophote shift as a perturbation due to the (phase shifted) gas ring; thus it should extend out to the radius of the ring. However, the most important point is that the bar ends at a finite radius *inside* the ring

(cusped isophotes). Therefore we consider the interpretation of Shaw et al as less plausible.

In Sect. 4 we will present models of the central photometry and discuss the nature of the barred component in more detail. We will give arguments that it is indeed a bar. In the following we will therefore call it a 'bar' for (semantic) simplicity.

The I image was calibrated using the standard stars (M 67) and comparing with the aperture photometry from de Vaucouleurs & Longo (1988).

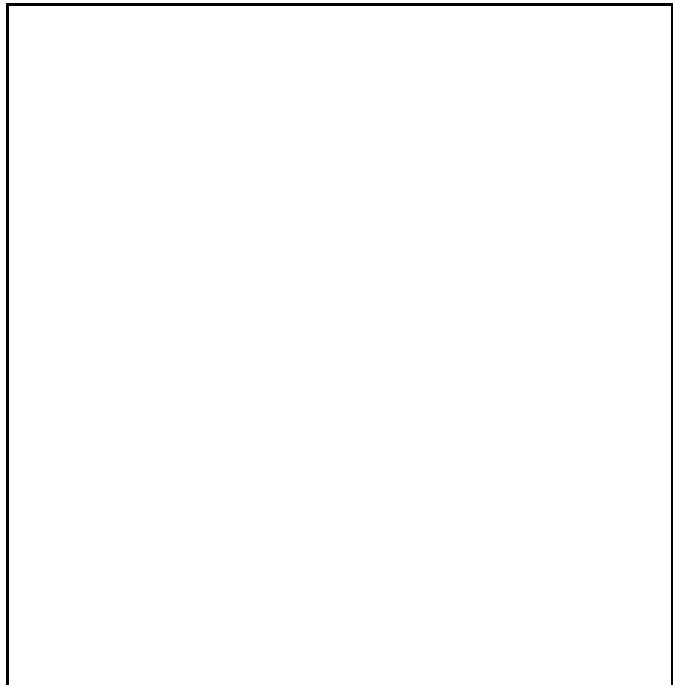


Fig. 1. Central region of M 94 (NGC 4736), I filter, 78×78 arcsec, north is up, east to the left. A logarithmic saw-tooth lookup table was used to produce this image, which shows isocontours as dark lines and the shallow gradients in between as different gray shadings. The cusped deformations of the isophotes due to the central bar at $P.A. = 28^\circ$ are easily visible.

3.2. NIR surface photometry

The data reduction of the J, K images proceeded as follows: To each triple of sky exposures a vertical median filter was applied, thus removing the stars. These sky frames were obtained for each galaxy and each filter, they were subtracted from the 18 galaxy images respectively. Since the dark current of the MAGIC camera is very low (Herbst et al 1993) it was not corrected for. The internal accuracy between *all* sky exposures of one night in each filter is better than 0.2%, with larger deviation from night to night. Therefore the flat field images were constructed for every night separately, using all sky images in each filter of that night. After flat field division of the 18 galaxy frames

the relative offsets of the galaxy centers and of stars (if present) were measured. Then the images were added together pixelwise, applying their individual offsets. An internal comparison allowed us to reject the bad pixel values. The J , K images look very similar to the I image (Fig. 1), showing the same behaviour of the isophotes and the bar feature. This is another support for the statement that the bar is not a feature due to dust absorption.

3.3. Isophote fits

After masking of disturbing field stars the isophotes of the I , J , and K images were fitted by ellipses (Bender & Möllenhoff, 1987). The results for the K image and the I focal reducer image are shown in Fig. 2 in the left and right panels respectively. The upper plots show the surface brightness in the inner part (left panel, K , $r < 90''$), and out to the largest radius we could obtain (right panel, I , $r < 450''$). As already stated by Boroson (1981) and Kormendy (1982), M 94 shows a steep non-exponential profile in the inner disk region ($r < 200''$). An exponential profile can be fitted only in the very outer disk. However, this region of steeper profile is still a disk in the kinematical sense: as will be seen later from the stellar velocity dispersion data, the real bulge of M 94 extends only to $\approx 20''$ radius. The steep disk profile is not totally smooth, it shows two 'shelves' at $r \approx 45''$ and $r \approx 120''$ which, according to Kormendy (1982) are characteristics of oval disks. These 'shelves' can be detected in all our visual and NIR surface brightness profiles.

The next plots in Fig. 2 show ellipticities $\varepsilon = 1 - b/a$ and position angles of the isophote fits to the K and I images. The curves are very similar in the different colors which means that dust does not play a role in M 94 (cf. Sect. 3.6). Due to the bar structure the ellipticity profile has a first maximum of $\varepsilon = 1 - b/a = 0.22$ at $\approx 10''$ radius (Fig. 2, left panel), the position angle is $P.A. = 28^\circ$ there. In the transition zone between central bar and outer disk at $r \approx 20''$ radius the isophotes are nearly round ($\varepsilon \simeq 0$). Then ε increases again, accompanied by a strong variation of $P.A.$ between $20''$ and $30''$. With increasing radius, the ellipticity increases generally from 0.2 to 0.25 at $r \approx 120''$, and to ~ 0.4 at large radii. The general slope of $1 - b/a$ is only interrupted by two local maxima in the ellipticity at $50''$ and $125''$, followed by a slight local decrease of ε . These maxima correspond to the two shelves of the surface brightness at $45''$ and $120''$. The main point here is, that $\varepsilon \approx 0.18$ between $r = 50$ and $100''$ and $\varepsilon \approx 0.23$ between $r = 120$ and $220''$. As Kormendy (1982) mentioned, these nested elliptical regions of different ε indicate, that at most one of these zones can be axial symmetric. Since warps can be excluded at this high surface brightness (Fig. 2), part of the disk must be oval. If we assume the zone between $r = 50$ and $100''$ as axial symmetric, we get an inclination angle of $i = 35^\circ$. Then the outer zone between $r = 120$

and $220''$ must be intrinsically elliptic with an axial ratio of $b/a \approx 0.9$.

The bottom plots of Fig. 2 show the a_4 -Fourier coefficient which quantifies symmetric deviations of the real isophotes from ellipses (Bender & Möllenhoff 1987). A positive a_4 value marks cusped isophote deviations; they are especially strong at $r = 10''$ (left panel, K). a_4 is large and positive in the limited radius between $r = 5''$ and $15''$; this suggests that the bar ends at $r \approx 15''$, well inside the star formation ring at $r \approx 45''$. Then a_4 shows an oscillating structure with increasing radius; at $45''$ and $110''$ we observe a change from slightly negative a_4 values (i.e. boxy deviations) to positive values. This finding is another confirmation of the structural changes in the disk of M 94 at $r \approx 45''$ and $r \approx 120''$ (right panel, I).

3.4. Fit of the surface brightness profile

To study the light distribution in the inner part of M 94 we used the I Cassegrain focus image, since with $0.46''/\text{pix}$ it has a better pixel-resolution than the J , K images with $0.66''/\text{pix}$. However, the I image is still smoothed by atmospheric seeing, which was determined from stellar images to a value of $1.76''$,

In first test fits of the surface brightness a de Vaucouleurs profile was found too steep while a Hernquist (1990) profile already gave a fairly good fit. For a better modelling we proceeded in a more general way, making use of the γ -profiles described by Dehnen (1993). They are characterized by a central luminosity density slope $\sim r^{-\gamma}$ and a length scale α . They include profiles between a steep Jaffe type ($\gamma = 2$), de Vaucouleurs type ($\gamma = 1.5$), Hernquist type ($\gamma = 1$), to a flat core type profile ($\gamma = 0.5$).

For a number of different values of slopes γ and length scales α we constructed a series of two-dimensional images from a model disk of the corresponding profile, seen under the inclination of M 94 ($i = 35^\circ$ determined from the surface photometry of the inner disk, see Sect. 3.3). For this modelling we chose a high pixel-resolution of $1 \text{ pix} \hat{=} 0.25''$. These model images were then convolved with a Gaussian seeing profile of $\text{FWHM} = 1.76''$. Then an ellipse fit was applied to every model image. In this way we obtained a two-parametric manifold of curves ($\gamma = 0.7, 0.8, \dots, 1.7$ and $\alpha = 12, 15, 17, 20, 25, 30''$) which we compared with the observed ellipse fit curve. Fig. 3 shows the profiles of a γ -series for $\alpha = 15''$ against $\log r$ compared to the observation. The best fit for the inner region $r \leq 30'' - 40''$ was the curve for $\gamma = 0.9 \pm 0.05$ and for $\alpha = 15 \pm 1.5''$. This is very similar to Hernquist's (1990) luminosity profile, which corresponds to $\gamma = 1$. For the outer part of the model disk we added a simple exponential profile with $r_e = 60''$ and neglected the oval shape of the outer disk. This is justified since our model disk is intended mainly for the inner region of M 94, near and inside the inner ring.

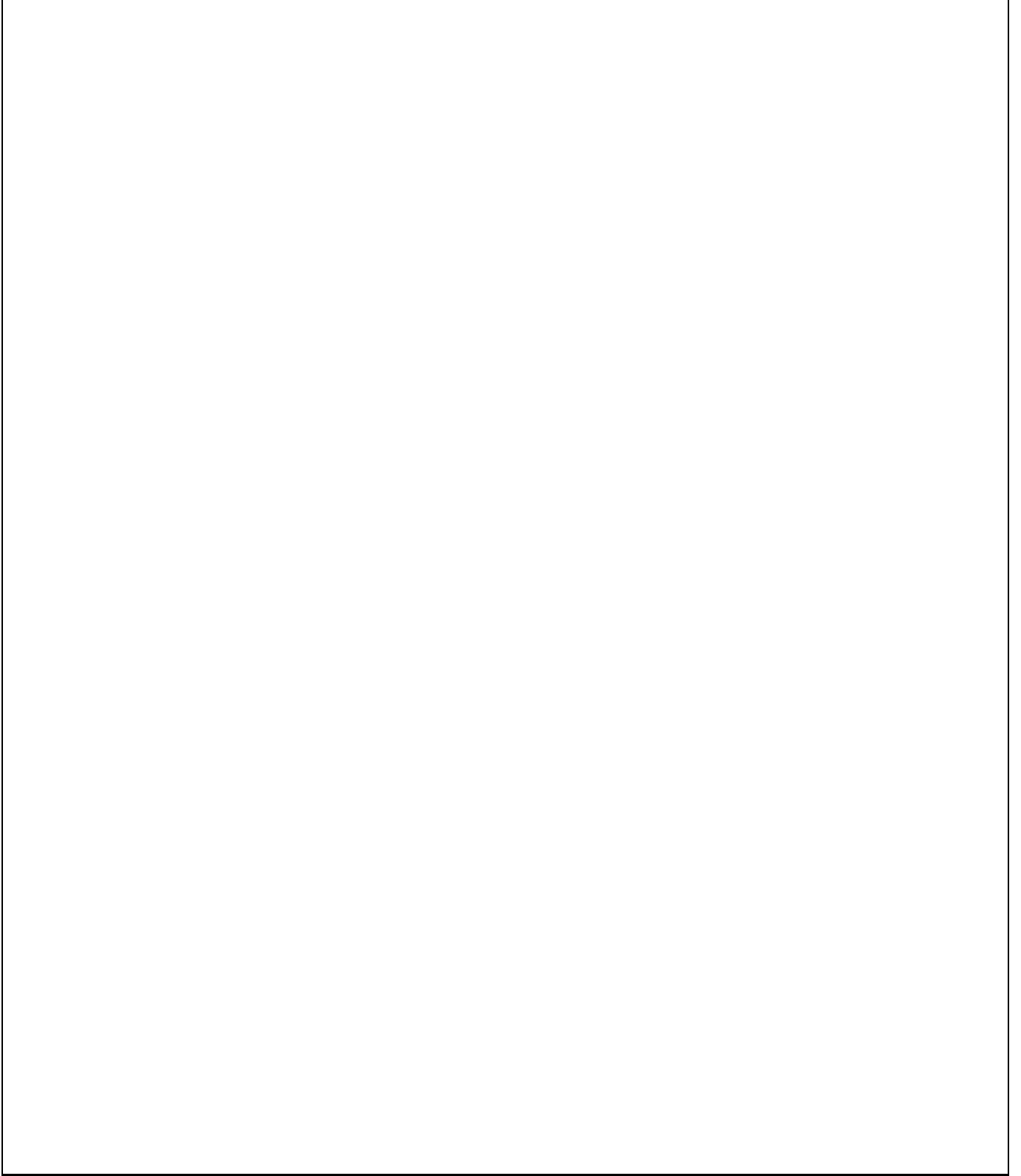


Fig. 2. Results of the isophote fits to the K image (left panel) and the focal reducer I image (right panel). The plots show surface brightness, ellipticity, position angle, and the a_4 -Fourier coefficient over radius. The central bar causes a first maximum of the ellipticity at $\approx 10''$ radius with a position angle $P.A. = 28^\circ$ (left panel, K). For $r > 45''$ (outer disk) the ellipticity increases slowly from 0.2 to 0.4, the $P.A.$ decreases from 120° to 90° (right panel, I). The structural changes in the disk at $\sim 45''$ and $\sim 120''$ can be seen in all plots.

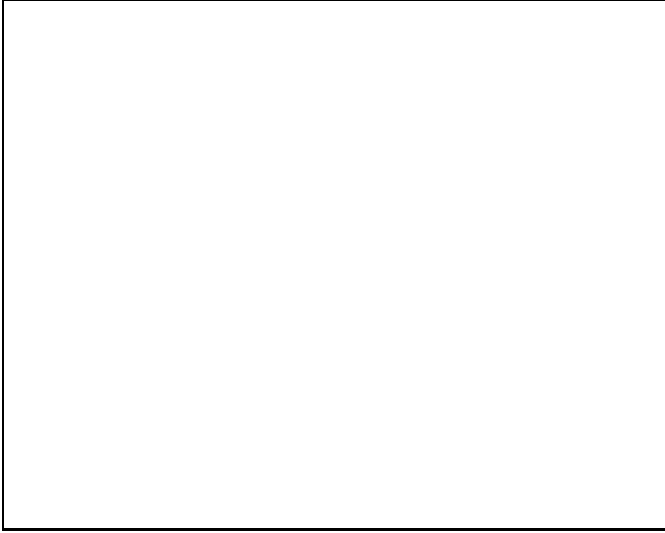


Fig. 3. Seeing-convolved γ -profiles with $\alpha = 15''$ for different γ -values compared to the observed I -profile. The curve for $\gamma = 0.9$ gives the best fit for $r \leq 40''$.

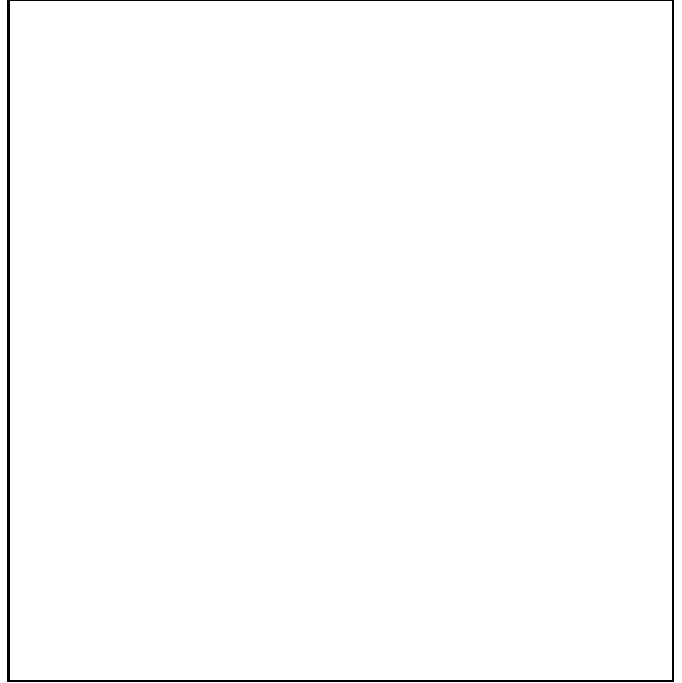


Fig. 4. H_α image of M 94, 2×2 arcmin, north is up. The continuum was subtracted using an appropriate red image. Emission of warm gas is present in the ring and in a central region which coincides roughly with the bar.

3.5. Distribution of the optically emitting gas

What is the distribution of the warm ionized gas in M 94? For that purpose a CCD image with an H_α filter was exposed. Since this image still contains a strong continuum contribution, we used the I frame as our most appropriate continuum image. Since both images have different pixel sizes, we rebinned the H_α image (27μ pixels) to the pixel size of the I image (22μ). Then both images were centered to ~ 0.1 pix and were subtracted with an appropriate intensity scaling which made the pure continuum regions vanish. Fig. 4 shows the result, it is very similar to Fig. 4d in Pogge (1989). The main H_α contribution comes from the well known ring of star forming HII regions. There exists also a central component of irregular, elongated shape; this extends mainly parallel to the stellar bar (compare also the H_α map in Duric & Dittmar, 1988). A weak and also irregular spiral structure can be detected between the ends of the bar and the strong ring at $r = 45''$. The defects in the very center are due to the different seeing during H_α and continuum exposures.

3.6. Color index images

$V-I$, $I-K$, and $J-K$, color index images were produced to study the morphology of dust absorption in M 94. The two respective images were rebinned, if necessary, to the same pixel scale. Then they were adjusted in position to an accuracy of < 0.1 pixels and divided in order to obtain a color index image. Dust reddening is present in the dark shaded regions in the color images. Fig. 5 shows, as example, the $I-K$ image. There is some dust present in circular arcs around the center, especially in the NE and W. These features seem to be correlated with the faint spiral arms

around the central bulge. They can also be detected in the $B-V$, $V-R$ images in Beckman et al (1991, Fig. 7a,b). Further out two spiral-arm-like dust features follow the ring of HII regions. All these dust structures can already be seen in the B broad band image in Beckman et al (1991, Fig. 8). The most important point here is that the inner dust arcs are situated near the long axis of the bar; they would not be able to produce the bar feature by an adequate extinction of a non-barred central stellar distribution in M 94.

3.7. Stellar kinematics

The CCD images of the stellar absorption spectra (4500–5400 Å) were reduced using the standard procedure with bias subtraction and flatfield division. A special mask function was constructed from a series of many differently exposed dome flats in order to correct for the intensity-dependent additive column offsets of the RCA chip at low light levels. The light distribution along the slit was corrected to a flat profile by means of an appropriate function obtained from skyflat exposures. The images were filtered to remove cosmetics and then rebinned row by row in $\log \lambda$ (equidistant in Δv). The spectra were centered and placed exactly parallel to the rows. During observation we had obtained two spectrograms for each slit position. Now the reduced spectrograms of each pair were coadded with an algorithm which removed further defects and

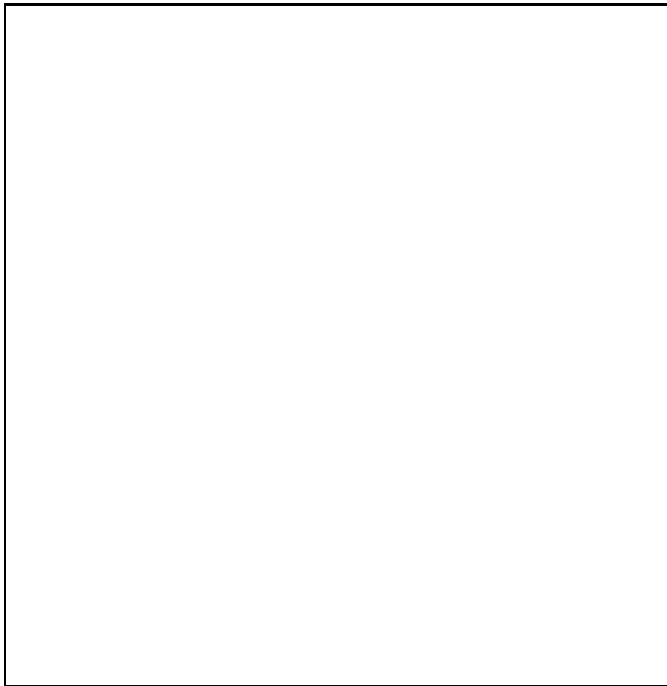


Fig. 5. Color index image $I - K$ of the central parts of NGC 4736 (M94), 2×2 arcmin, north is up. There exist some dust-reddened arc regions near the center (dark shaded), however they are not responsible for the deformations of the isophotes in the I image. Long dust lanes of spiral arm shape are crossing the ring of HII regions at $r \approx 45''$.

remaining cosmics. The continuum was subtracted by applying a polynomial fit to every row. The H_{β} - and $[OIII]$ -lines were masked to avoid disturbances by the emission lines. Then the spectrograms were prepared for the cross-correlation by applying a *cos*-bell function to their ends. A similar technique was used for the preparation of the template spectra of several G8 III, K0 III, K3 III, and K5 III stars.

The stellar rotation velocity and the velocity dispersion of the galaxy were determined by a Fourier-cross-correlation technique with a standard template star; it is described in detail in Bender (1990). This technique allows one also to obtain the line-of-sight velocity distribution of the stars.

Fig. 6 shows the resulting stellar rotation (lower panel) and stellar velocity dispersion (upper panel) along the four slit orientations $P.A. = 0^\circ, 45^\circ, 90^\circ, 135^\circ$. The strongest rotation amplitudes are seen along $P.A. = 90^\circ$ and 135° . Since the latter amplitudes are nearly equal, the kinematic line of nodes must be at $\sim 113^\circ$ and the rotation axis at $P.A. \approx 23^\circ$. The stellar rotation velocity increases nearly linearly to $r = 12''$ and then remains on that level until $r \approx 60''$. For larger radii our signal is too weak for a reliable result from the cross-correlation analysis. The curves become noisy for $r > 40''$, this is due to template mismatching in the ringlike zone of star formation.

Under the assumption of circular symmetry the stellar velocity field can be easily deprojected. If this assumption is justified, and all 4 rotation curves are deprojected with the same correct inclination with respect to the correct line of nodes, than the deprojected rotation velocity curves should fall together. If the adopted inclination and line of nodes are choosen incorrectly, the projected curves are different. In this way we determined by iteration $i = 30^\circ \pm 5^\circ$ for the inclination, and a position angle of $P.A. = 113^\circ \pm 1^\circ$ for the line of nodes. The deprojected rotation curves coincide quite well, especially outside the bar. From the superposed projected curves it is possible to calculate a mean stellar rotation curve with a better signal-to-noise-ratio (see next Section). This 'kinematic' inclination angle is very similar to that obtained by surface photometry of the inner region of the disk ($i = 35^\circ$ between $r = 50$ and $100''$, see Sect. 3.3).

In the stellar velocity dispersion profile (upper panels of Fig. 6) we see a rather sudden increase inside $r = 20''$ to the central value of $\sigma_o = 120 \text{ km s}^{-1}$. This is most plausibly interpreted as the signature of a small central bulge with $r \approx 20''$ in M94. Outside the bulge we obtain $\sigma = 60 \text{ km s}^{-1}$, a value which is determined by our spectral resolution and is probably higher than the velocity dispersion of the disk. The extent of the bulge is fairly independent of the slit orientation, therefore its shape is nearly axially symmetric.

The broadening function of the stellar absorption lines in a galaxy spectrum is produced by the local velocity distribution integrated along the line of sight. The broadening function is gaussian only for simple dynamic systems; in general it is a more complex function, which we call the line-of-sight stellar velocity profile (LOS-SVP). we use the method of Bender (1990) to determine this function by a deconvolution of the correlation peaks. Fig. 7 shows the line-of-sight stellar velocity profiles of the spectra along $P.A. = 90^\circ$ at different radial distances from the center ($0'', \pm 5'', \pm 10'', \pm 20''$). While the central profile is broad and gaussian (bulge profile), the line profiles at $\pm 5''$ are already asymmetric. At $\pm 10''$ the profiles are more complex: we see a narrow peak from the rapidly rotating disk-stars, superposed onto a broader, more slowly rotating component from the bulge stars. At this radius the contributions of disk and bulge are approximately of the same magnitude. At $\pm 20''$ only the disk profiles are visible on both sides.

These line-of-sight velocity profiles confirm the existence of a bulge of $\sim 20''$ radius in M94. Kormendy (1993) used the old kinematical data of Pellet & Simien (1982) to argue from $v_{rot}/\sigma \approx 0.75$ and $\varepsilon \approx 0.1$ that M94 has no bulge but is disklike even in the center. This argument is no longer valid since we now know that it compares velocities from two different components. From the velocity decomposition in Fig. 7 we see that at $r = \pm 10''$ the bulge component has a much smaller rotation velocity than the disk component; thus v_{rot}/σ for the bulge

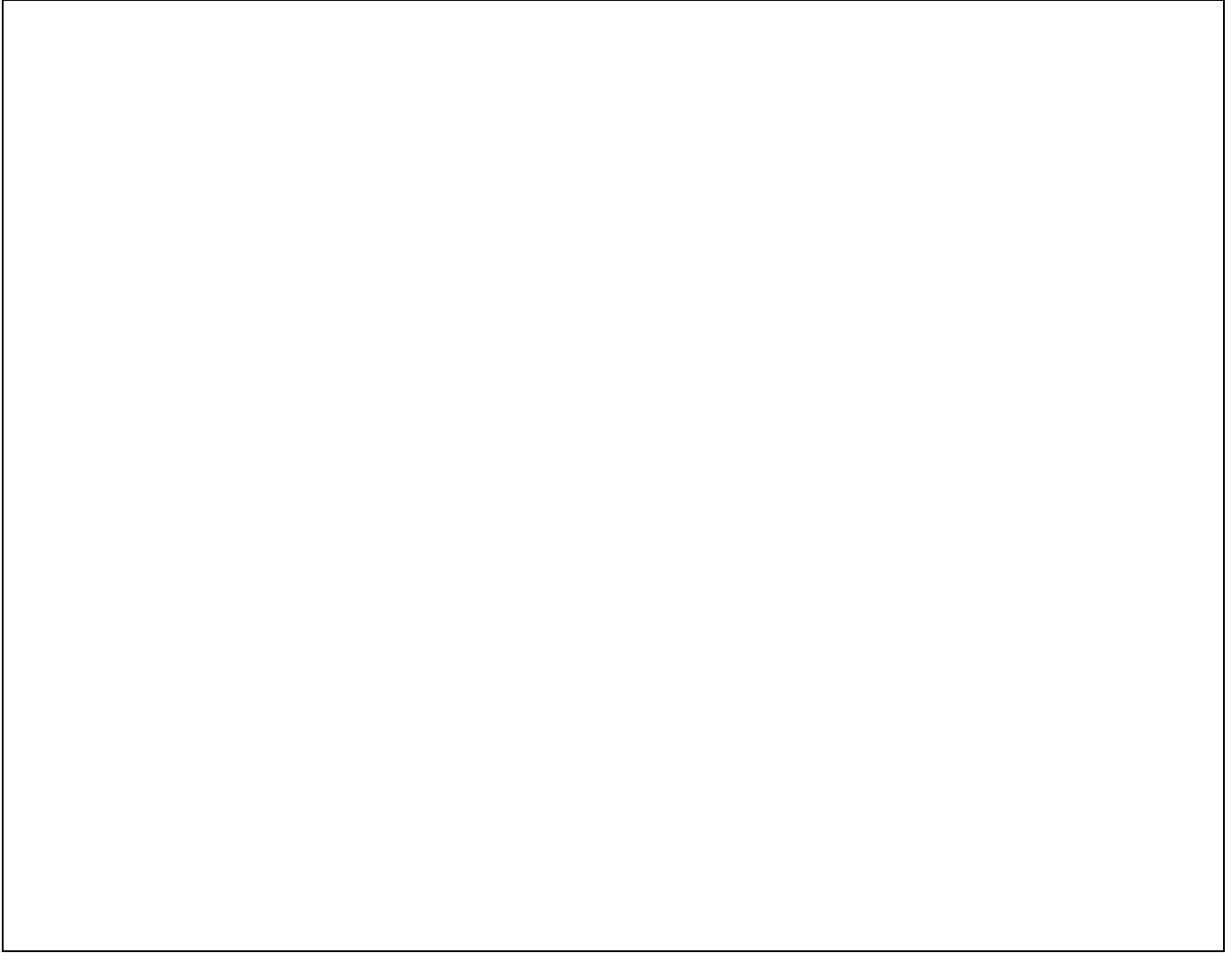


Fig. 6. M94: Stellar velocity dispersion (top) and stellar rotational velocity (bottom) along $P.A. = 0^\circ, 45^\circ, 90^\circ, 135^\circ$. The kinematical influence of the small bulge extends only to $r \approx 20'' \hat{=} 600\text{pc}$.

stars becomes much smaller, and is not in conflict with the classical $v_{rot}/\sigma - \varepsilon$ - diagram. Furthermore it should be emphasized that spiral structure is not detectable inside the bulge radius ($20''$) of M94 (e.g. Fig. 5).

3.8. Emission gas kinematics

The reduction of the emission line spectra was performed in a very similar way as described above for the stellar spectra. In order to extract the emission lines from the stellar continuum, the latter was subtracted via a polynomial fit (with masked emission lines) in every row. The velocity field of the gas is then easily measurable in the H_α , $[NII]$, and $[SII]$ emission lines. The radial velocity of the gas was determined by cross-correlation with the emission line spectrum from the galaxy center. Since there the H_α emission is compensated by the absorption of the stellar continua, we also used as templates spectrograms from

the star forming rings (and correcting for their rotational offset).

Fig. 8 shows the resulting gas rotation curves for all 8 observed slit orientations. To compare the gas velocities with the stellar rotation field we use the mean stellar rotation curve from the last Section and project it along the corresponding slit position angles. This results in the solid lines in each panel of Fig. 8. The rotation curves of gas and stars show a similar general trend, i.e. practically disk dominated rotation for both components, however, with some marked differences. They are best studied by subtraction of the mean *stellar* rotation from the gas velocity curves for each slit orientation.

(1) Inspection of the velocity residuals shows that the gas velocities are systematically higher than the stellar mean velocities. These systematic differences are not an artefact of our mean stellar rotation curve, they can be seen directly by comparing measurements of gas and

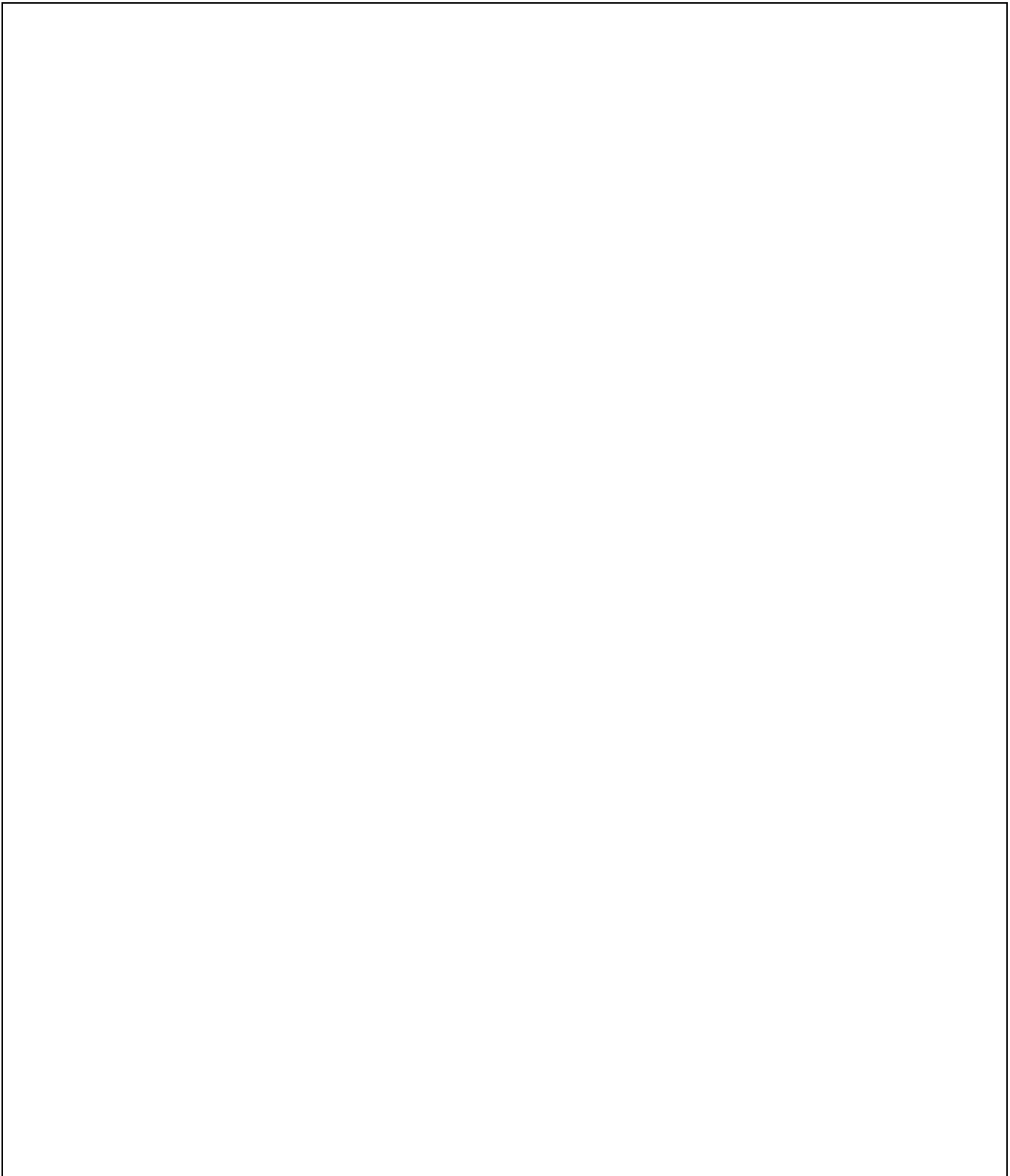


Fig. 8. M94: Rotational velocity of the gas (circles) along 8 different slit positions, marked in each panel. The bulk rotation of the gas is similar to the stars (solid line). However, the gas rotates faster and shows additional humps and dips in the curves.

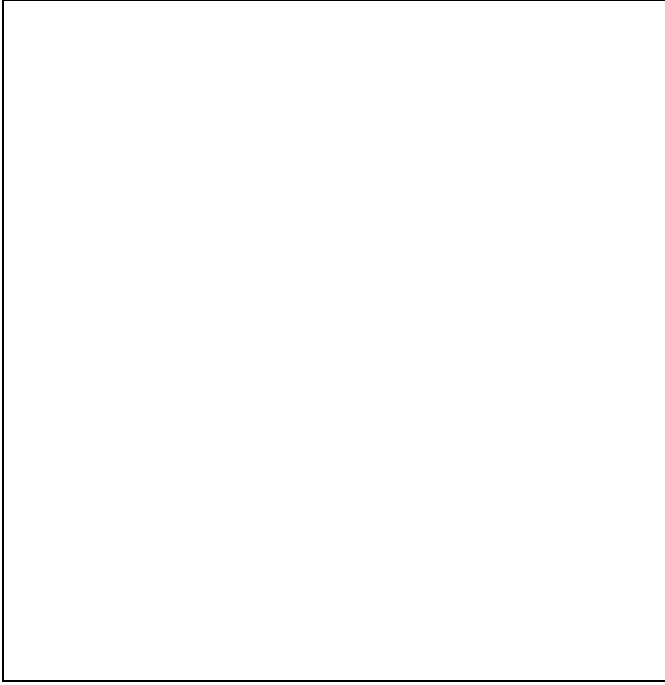


Fig. 7. Line-of-sight stellar velocity profiles (LOS-SVP) along $P.A. = 90^\circ$ at different radial distances from the center ($0''$, $\pm 5''$, $\pm 10''$, $\pm 20''$). While the central profile is broad and gaussian (bulge profile), the influence of the bulge decreases with distance from the center. The combined profile at $\pm 10''$ shows the broad, non-shifted bulge profile and the rotationally shifted narrow disk profile. At $\pm 20''$ only the narrow disk profile can be seen.

stellar rotation for the common position angles $P.A. = 0^\circ, 45^\circ, 90^\circ$, and 135° . Several interpretations are possible.

(i) The gas rotates intrinsically faster than the stars.

(ii) A second possibility could be a different rotation axis for stars and gas. As we have seen in the last section, the best-fitting inclination of the stellar rotation plane is $30^\circ \pm 5^\circ$. A simple increase of the inclination of the gas orbits to $\approx 45^\circ$ and a slight change of the line of nodes could explain the general trend (assuming circular gas orbits), but this would mean that the gas rotates in an inclined orbit with respect to the stellar rotation which is a rather unplausible suggestion.

(iii) A third possibility is that the gas moves on elliptic orbits along an axis roughly parallel to the small central bar. Deviation of the gas orbits from circular motion were already discussed by van der Kruit (1976), when he measured the gas velocities in the H_α -ring. Strong deviations from the pure circular motion of the HI gas were also observed by Mulder & van Driel (1993) in the form of variations in inclination and the line of nodes of the HI velocity field. Our observed maximal amplitude of 120 km/sec for the gas velocities at $P.A. = 118^\circ$ between $r = 20''$ and $40''$

matches well to the corresponding HI velocities in Mulder & van Driel (they use $i = 40^\circ$ in their Fig. 12b).

A further plausible explanation of the systematic differences between stellar and gas rotation is given in Sect. 5.

(2) In the gas rotation curves there appear 'overshooting' and 'counter-rotating' humps and dips of the gas velocity near the center of the galaxy. Fig. 9 shows the location of these local deviations by filled (humps) and open (dips) circles. Since many of them occur at similar radii ($10''$ to $20''$) for different position angles, we conclude that the reasons for these local deviations are of nearly circular shapes, probably spiral arms. The eastern arc of filled circles (redshifted deviations with respect to the general velocity field) can roughly be identified with the corresponding dust arcs displayed in the $I - K$ image (Fig. 5). However, there also seems to be some connection with the bar: The deviations occur mainly along the long sides of the bar and they are mostly positive on the eastern side and negative on the western side. In contrast to the general trend these deviations can not be eliminated by a variation of the inclination angle and/or the line of nodes.

A comparison with the dynamical model will be given in Sect. 5.6, the discussion of the results in Sect. 6.

4. Morphological model: Central bar or triaxial bulge?

In Sect. 3.1 we described the isophote twist, the variations of the ellipticity, and the occurrence of cusped isophotes in M 94 inside $40''$ (Fig. 1 and Fig. 2). It could be shown from the $I - K$ color index image that these are not an effect of dust absorption. Are the isophote twists etc. the signature of a bar which is a disk phenomenon, are they caused by a triaxial bulge, i.e. a structure extended in z -direction?

For the construction of a morphological model of the inner region of M 94 we have to consider the following observational facts:

- a) isophote twist of nearly 90° between $15''$ and $25''$
- b) round isophotes inside $10''$ which can not be explained just by seeing
- c) cusped isophote shapes at $r \approx 15''$
- d) increased stellar velocity dispersion inside $20''$, independent of the position angle.

We present two different models for the interpretation of these observational findings: (1) M 94 consists of a disk and an axisymmetric (spheroidal) bulge, the isophote twist and the cusped shapes of the isophotes are due to a weak additional bar component. (2) M 94 has a triaxial bulge in the center which is responsible for the isophote twist (no direct explanation for the cusped isophote deviations).

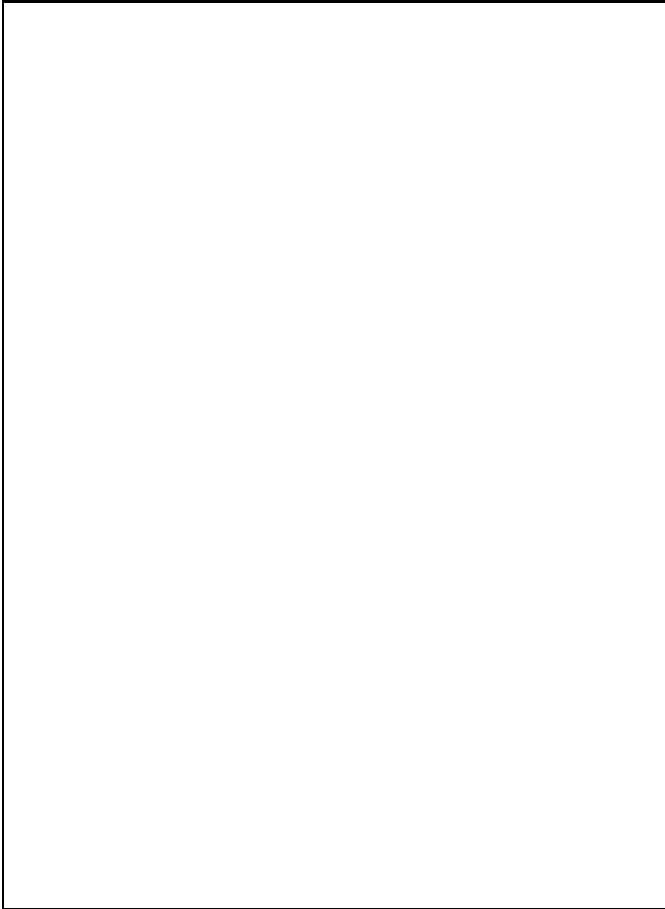


Fig. 9. M94: Locations of the humps and dips in the gas rotational velocities relative to the mean stellar rotational velocities along 8 different slit positions. Open circles refer to negative, filled circles to positive residual velocities, their diameter gives the absolute values. The deviations concentrate along circular arcs, probably connected to the inner spiral structure.

4.1. Axially symmetric bulge, disk, and bar

This model with an axisymmetric bulge is supported by the fact that the stellar velocity dispersion profile is identical for 3 of 4 slit orientations. The σ - profile along $P.A. = 135^\circ$ is somewhat broader; however, we do not consider this as significant.

Since we are mainly interested in the structure of the inner kpc, we assume that the entire disk of M94 is axisymmetric and neglect its outer oval shape. The modelling proceeded as follows: According to the isophote ellipse fits a seeing-convolved $\gamma = 0.9$ (Dehnen & Gerhard 1994) model for the inner disk (plus bulge), and an outer exponential disk component were constructed. This two-component model together with an additional constant value for the sky background fitted the whole disk of M94 very well. The model parameters for the inner disk were: $\gamma = 0.9$, length scale $\alpha = 15''$, and from the surface pho-

tometry of the inner disk region (Sect. 3.3): inclination angle $i = 35^\circ$, position angle $P.A. = 113^\circ$.

This model was convolved with a Gaussian of FWHM = $1.76''$ according to the seeing during observation (measured from the point spread function of stars in the I -image). For the outer disk we adopted an exponential profile with $r_e = 60''$, with inclination and position angle as above. The central intensity was adjusted to the I image.

When this model was subtracted from the observed I image, a central barred component remained, with a fairly flat profile. Figure 10 shows the residual central bar. The size of the bar is about $30 \times 14''$ in projection. At the distance of NGC 4736 ($D = 6.6$ Mpc, $1'' \hat{=} 32pc$) and for an inclination of $i = 30^\circ$, the size of the bar from end to end is $42 \times 14''$ or 1.3×0.45 kpc.

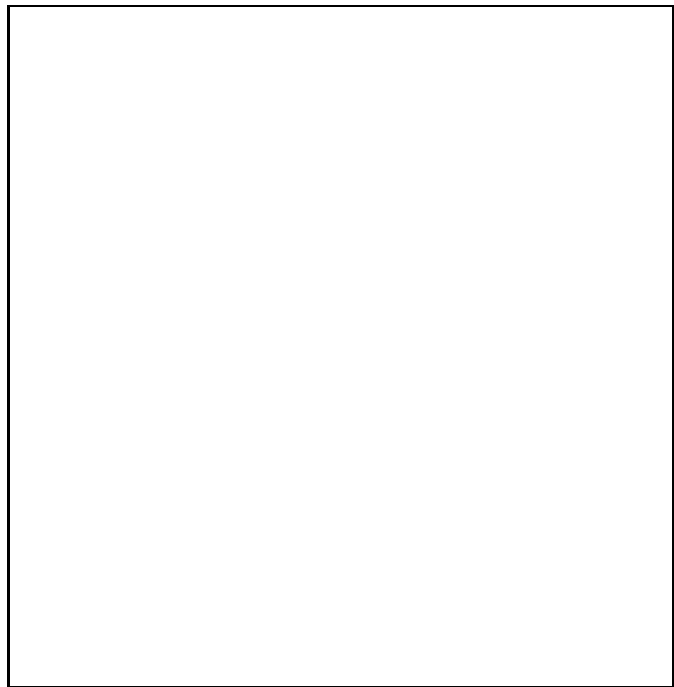


Fig. 10. Residual central bar component in M94 after the subtraction of a two-component model for bulge ($\gamma = 0.9$) and exponential disk. The size of the bar is $30 \times 14''$ in projection. The scale is the same as the I image in Fig. 1 ($78 \times 78''$, north is up).

In a second step the central bar itself was modelled. As Fig. 10 shows, the luminosity profile along the bar is rather shallow in the center and steep at the boundaries. Therefore an elliptical $r^{1/4}$ profile is not adequate. A flatter Ferrers profile (Ferrers 1877) was chosen. It has the following elliptical surface brightness distribution:

$$\Sigma(m^2) = \begin{cases} \Sigma_0(1 - m^2)^n, & \text{if } m^2 < 1, \\ 0, & \text{else,} \end{cases} \quad (1)$$

where

$$m^2 = \left(\frac{x}{a}\right)^2 + \left(\frac{y}{b}\right)^2. \quad (2)$$

The parameter n determines the radial density profile, Σ_0 is the central surface brightness. The long and short axes of the bar are denoted by a and b , respectively. For our model we chose $n = 2$, $a = 15''$ and $b = 7''$ (in projection).

Fig. 11 shows the coadded model disk and Ferrers bar. Subtraction of this composite model from the I image left only very small residuals.

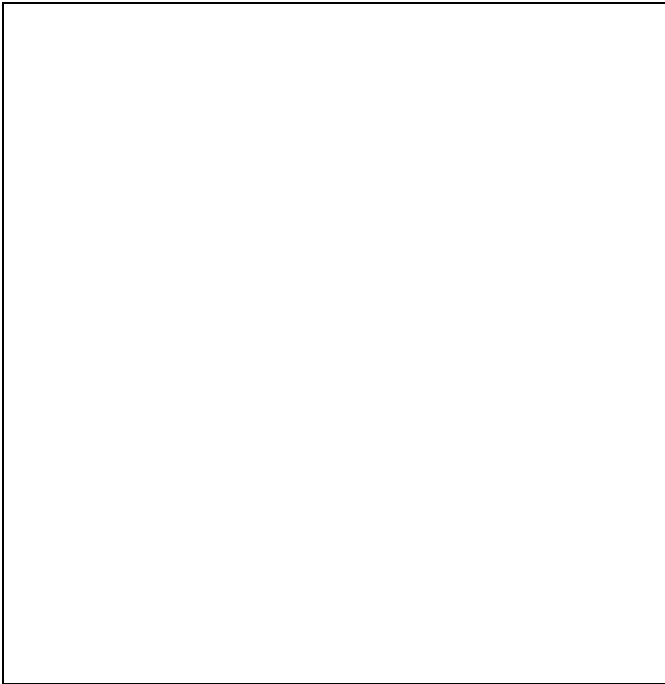


Fig. 11. Two-component model for the disk and bulge together with a Ferrers model for the central bar component in M94. Compare this composite model with the I image in Fig. 1; the same scale and lookup table were used.

4.2. Triaxial bulge and disk

One of the main characteristics of the above model is the fact that the overwhelming portion of the mass in the central region is contained in the axisymmetric component, which results in a dominant monopole component of the potential in the disk plane. Compared to this the quadrupole component due to the bar is only a minor perturbation of the order of a few percent. If the light in the inner $10''$ is dominated by a single triaxial component, this can therefore only have a small flattening in the disk plane of M94.

We have the following observational boundary conditions for the construction of a triaxial bulge:

- a) The long axis of the bulge is along $P.A. = 28^\circ$.

- b) From the line-of-sight-velocity decomposition (Fig. 7) we conclude that the amount of light from the bulge at $r \approx 10''$ is approximately equal to that of the disk there.

- c) From the σ - profile (Fig. 6) the bulge light inside $\sim 10''$ is dominant compared to the disk light.

The construction proceeded as follows: The azimuthally averaged luminosity profile from the ellipse fit to the observed I image (Fig 2) was fitted by a two-component model including a steeper γ - profile for the bulge and a flatter γ - profile for the disk. The contribution of these profiles had to be equal at $r \approx 10''$, and their sum had to fit the observed total profile. A good solution was found with $\gamma = 0.9$ and $\alpha = 15''$ for the bulge component, $\gamma = 0.8$ and $\alpha = 205''$ for the disk component, with a ratio of their total light B/D = 1.044. It is obvious that these two components have a rather similar structure. Furthermore this decomposition is not unique and the astrophysical meaning of the labels 'bulge' and 'disk' for these components is not clear.

Using these profiles we constructed the projected image of an elliptical prolate bulge with $b/a \approx 0.3$ and its long axis along $P.A. = 28^\circ$ and an inclined disk ($i = 35^\circ$, node line along $P.A. = 113^\circ$) and coadded their projection as a twodimensional model image of M94. The result was not a good description for M94, since the bulge component was too dominant to give the correct isophote twist at the correct radius. The same is true with a centrally flatter disk profile. Vice versa, if we weakened the bulge component or made its profile steeper, we could not satisfy above conditions b) and c). A number of different bulge axis ratios and bulge-disk combinations were tried. The most serious difficulty is that a bulge with a density profile as above has no sharp boundary, even though the bulge profile steepens to r^{-4} for $r \gg 15''$. Therefore no cusped isophotes are produced. A bulge does not have a natural outer radius like a bar at its corotation radius. Of course, it would be possible to use more complex components, e.g. a triaxial bulge with changing axis ratios or a bulge which is not elliptical or which has a sharp outer boundary. However, then too many arbitrary parameters would come into play and the result would not be very meaningful.

We conclude that our first model is the most plausible: M94 consists of a disk with a Hernquist like profile ($\gamma \approx 1$) and a spheroidal bulge which can only be separated from the disk by its stellar velocity dispersion but not by its light profile or color. The deviations and twists of the isophotes are due to a superposed weak bar component. The bar ends inside the gas ring at its corotation radius.

5. Dynamical model

In this section we present a model for the kinematics in the inner region of M94. We will try to explain the radial velocity curves of the stars and of the gas emission, espe-

cially of the 'overshooting' and 'counter-rotating' components (humps and dips, Fig. 6).

As was shown in Sect. 3.7 the rotation curves of stars and gas are qualitatively similar. The velocity dispersion of the stars outside $r = 20''$ is below 60 km s^{-1} , which is the observational limit. So we can assume that the kinematics of the stars outside the bulge region is disk-like. For the bulge we have a projected stellar rotation velocity $v_{rot} \approx 50 \text{ km s}^{-1}$ and a velocity dispersion $\sigma \approx 120 \text{ km s}^{-1}$ (Fig. 7). From the well known relations between ϵ and v_{rot}/σ we estimate a true flattening of $\epsilon \approx 0.4$ for the bulge.

5.1. Mass model

We construct our mass model according to the morphological components from Sect. 4.1:

- The bulge and inner disk is approximated by a flattened γ -model with $\gamma = 0.9$, $\alpha = 15''$, and $q = 0.6$.
- The bar component is approximated by a Ferrers bar: $a = 20.8''$, $b = 7.3''$, $n = 2$.
- The contribution of the outer exponential disk for the mass model of the inner bar region is neglected.

The mass-to-light-ratio ζ was determined by fitting circular orbits at $r = 45''$ (inner ring) and was assumed to be equal for both components (no systematic color gradient was observed).

The flattened γ -profile for the inner disk and bulge is:

$$\rho_q(p) = \frac{M}{2\pi q} \frac{\alpha}{p^\gamma} \frac{1}{(p + \alpha)^{4-\gamma}}, \quad (3)$$

with $p^2 = x^2 + y^2 + z^2/q^2$, scale-length α , and $M = 2 \times 10^{10} M_\odot$.

The mass of the bar can be calculated by integrating the bar surface brightness (Eq. 1) over all space:

$$M = \zeta \iint \Sigma(m^2 = \frac{x^2}{a^2} + \frac{y^2}{b^2}) dx dy \quad (4)$$

$$= 2\pi\zeta \Sigma_0 ab \int_0^1 dr r(1-r^2)^n \quad (5)$$

$$= \zeta \Sigma_0 \pi ab \frac{\Gamma(n+1)}{\Gamma(n+2)}, \quad (6)$$

where the last integral was evaluated by using integral tables (e.g. Bronstein & Semendjajew, 1987, 1.1.3.4 #39).

Using the values above one gets a bar mass of $9.8 \times 10^8 M_\odot$, which is about 14% of the mass of the flattened γ -model up to the end of the bar ($r = 20''$ in the plane of the galaxy, $7.0 \times 10^9 M_\odot$). From the surface photometry calibration we obtain $I = 7.8$ inside that circle. With the color indices of de Vaucouleurs & Longo (1988) for the inner $35''$ aperture of M94, we obtain $B = 10.6$ inside of $r = 20''$, and with a distance of 6.6 Mpc this leads to

$M/L_B = 1.8$. This extraordinary low value was already obtained by Buta (1988); it is a consequence of the extremely high surface brightness of M94. Fig. 12 shows the radial surface density of the different components of our model.

The bar rotates rigidly with a constant pattern speed Ω_b , which is determined in Sect. 5.4.

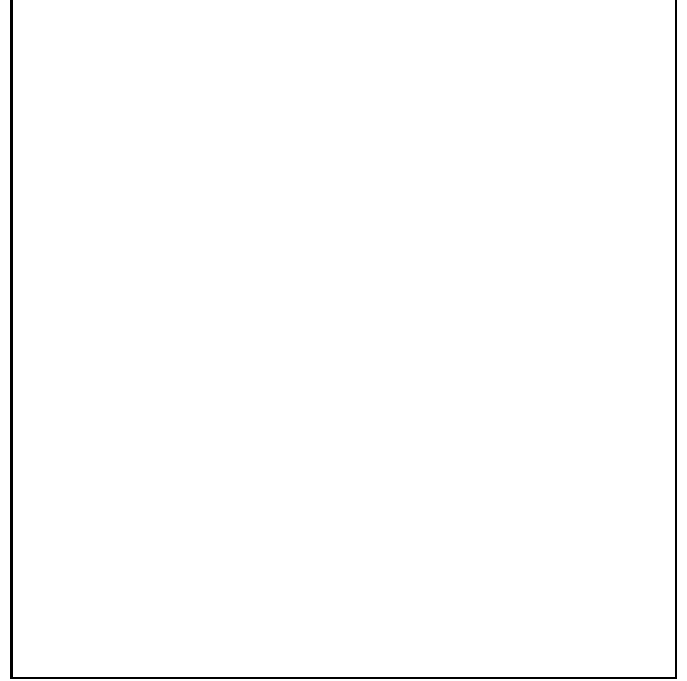


Fig. 12. Surface brightness of γ -model, Ferrers bar and their sum along the bar major axis in units of the characteristic length α .

5.2. Gravitational potential

To calculate the families of stable closed orbits one needs the potential of the galaxy model, from which one can determine the forces exerted on a test particle. The potential of the flattened γ -model (Dehnen & Gerhard 1994) is

$$\Phi_q(R, z) = -\frac{1}{2} \int_0^\infty \frac{\tilde{\psi}(\tilde{m}) d\tau}{(\tau+1)\sqrt{\tau+q^2}}, \quad (7)$$

where

$$\tilde{m} = \sqrt{\frac{R^2}{\tau+1} + \frac{z^2}{t+q^2}} \quad (8)$$

and

$$\tilde{\psi}(\tilde{m}) = \frac{1}{2-\gamma} \left[1 - \frac{\tilde{m}^{3-\gamma} + (3-\gamma)\tilde{m}^{2-\gamma}}{(\tilde{m}+1)^{3-\gamma}} \right]. \quad (9)$$

This expression was numerically calculated using a routine by Walter Dehnen, whereas the potential of the Ferrers bar was calculated with the following expansion method described by Binney & Tremaine (1987):

$$\Phi(r, \varphi) = \sum_{k=0}^{\infty} \sum_{m=-k}^k V_{km} Y_{km}(\arcsin(r), \varphi), \quad (10)$$

where the expansion constants V_{km} are given by

$$V_{km} = -\pi^2 G g_{km} \int_0^{2\pi} d\varphi' \times \int_0^{R(\varphi')} \Sigma(r', \varphi') Y_{km}^*(\arcsin(r'), \varphi') r' dr'. \quad (11)$$

The functions Y_{km} are the well known spherical harmonics, G is Newton's constant of gravity and the g_{km} are constants. The variable r is normalized in such a way that the density distribution lies inside a circle of radius 1. $R(\varphi')$ denotes the edge of the density distribution. The equations give the potential in a disk inside this circle. The expansion was truncated at $k = 30$ and $|m| = 8$; such high values were necessary to approximate the potential of the elongated bar in M 94 accurately enough (the axis ratio is 1:2.85). For rounder bars smaller values of k and $|m|$ are sufficient.

5.3. Resonances and families of closed orbits

The families of closed orbits in barred potentials are determined mainly by the loci of the Lindblad- and corotation-resonances (Contopoulos & Grosbøl, 1989). For weak bars linear theory can be applied. Then the resonances can be calculated in terms of two natural frequencies:

$$\Omega_0^2 = \left(\frac{1}{R} \frac{d\Phi_0}{dR} \right)_{R_0} \quad (12)$$

is the circular frequency of a star on a circular orbit with radius R_0 in the axisymmetric part of the potential (Φ_0). Small radial displacements from this circular orbit lead to radial oscillations with the epicycle frequency κ_0 , where

$$\kappa_0^2 = \left(\frac{d^2\Phi_0}{dR^2} + 3\Omega_0^2 \right)_{R_0}. \quad (13)$$

The frequencies Ω_0 and κ_0 are calculated only from the axisymmetric part of the potential and are accurate only for weak bars. The exact positions of the resonances in strong bars have to be determined from the behaviour of the families of closed orbits (see next section).

Azimuthal displacements do not change the circular orbit, so the azimuthal frequency is 0. The resonances arise between the forcing frequency seen by the star, $m(\Omega_0 - \Omega_b)$ (for barlike potentials $m = 2$), and the two natural frequencies κ_0 and 0.

If $\Omega_0 - \Omega_b = 0$, the *Corotation* resonance (CR) appears, because the star moves as fast as the rotating bar. If $m(\Omega_0 - \Omega_b) = \pm\kappa_0$, the star encounters successive crests of the potential at a frequency that coincides with that of the natural radial oscillations. An *Inner Lindblad* resonance (ILR) occurs if the star overtakes the rotating bar ('+'-sign), an *Outer Lindblad* resonance (OLR) otherwise ('-'-sign).

A *resonance-diagram* can be plotted (Fig. 13) and the loci of the resonances can be determined by drawing a horizontal line at Ω_b . The small oscillations in the curves near $r = 40''$ are numerical artefacts: To calculate κ_0 one has to evaluate the second derivative of Φ_0 . This axisymmetric part of the potential consists of the flattened γ -model and the axisymmetric part of the bar potential, which is given in a series. Even if the potential is approximated quite well, the second derivative still has oscillations, which are visible in Fig. 13.

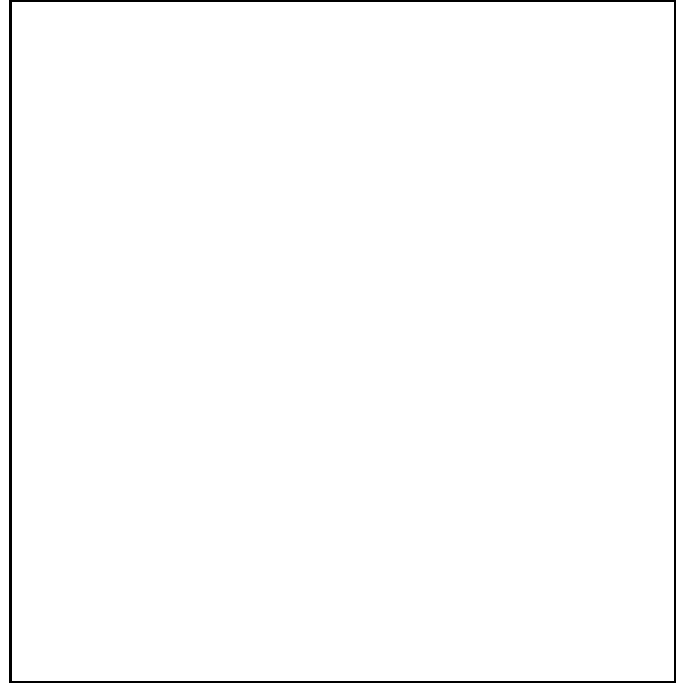


Fig. 13. Resonance diagram for our model. The horizontal line $\Omega_b = 2.5$ shows the resonances, which are marked below. The bar ends at $r = 20''$. The oscillations in κ are due to the numerically calculated second derivative of the potential with a limited order of the expansion.

The resonance diagram shows that because of the steep potential of M 94 only one inner Lindblad resonance can occur. In such a potential the closed orbit families in the corotating frame of reference have the following properties (see Contopoulos & Grosbøl, 1989 for a complete review):

The prograde x_1 -orbits are elongated along the bar and exist from the center outwards to nearly CR. These orbits should strongly sustain the stellar bar shape.

The prograde x_2 -orbits are elongated perpendicular to the bar and exist in the energy range all the way from the center up to the energy of the ILR.

The prograde x_3 -orbits have the same properties as the x_2 -orbits, but are unstable, so they can not be populated with gas and are not considered in the following.

The retrograde x_4 -orbits are not useful inside the CR, because they would lead to a retrograde streaming of gas, which is not observed.

However, outside the CR we have only retrograde orbits, which are nearly round. Inside the OLR they are slightly elongated perpendicular to the bar, outside the OLR along the bar. These orbits can be populated with gas, because a retrograde orbit outside CR has no retrograde streaming in the rest frame.

5.4. Pattern speed

The pattern speed Ω_b is the only free parameter in our model which can not be observed directly. Our aim was to determine Ω_b using the structure of the orbits of our mass model.

The stellar bar must be supported by x_1 -orbits. As these exist only inside CR, the pattern speed has to be so low that CR lies outside the bar (Sellwood & Wilkinson 1992). Two other constraints on the pattern speed are the location of the gas ring at $r \approx 45''$ and the gas-poor zone between $20''$ and $40''$. As was shown by Schwarz (1981) a rotating bar transports gas from the area between CR and OLR to or just beyond the OLR. To meet these two constraints, the pattern speed in our model was determined at $\Omega_b = 2.5$ in our units, corresponding to one revolution in 2.1×10^7 years or 290 km s^{-1} per kpc. In this way the OLR of the inner bar coincides with the ILR of the outer oval disk: the star formation ring at $r \approx 45''$ (Gerin et al 1991).

5.5. Kinematics of the stars

How do the observed stellar rotation velocity and the velocity dispersion in the bulge correspond to the observed mass distribution? The radial Jeans equation for an axisymmetric stationary system in the equatorial plane

$$-\rho \frac{\partial \Phi}{\partial R} = \frac{\rho \overline{v_R^2}}{R} \left[\left(1 - \frac{\overline{v_\phi^2}}{\overline{v_R^2}} \right) + \frac{\partial \ln \rho}{\partial \ln R} + \frac{\partial \ln \overline{v_R^2}}{\partial \ln R} + \frac{R}{\overline{v_R^2}} \frac{\partial \overline{v_R v_z}}{\partial z} \right] \quad (z=0) \quad (14)$$

(Binney, Tremaine 1987, p.197). Here R denotes the cylindrical radius. Assuming an isotropic rotator, we have

$\overline{v_R^2} = \overline{v_z^2} = \sigma^2$, $\overline{v_R v_z} = 0$, and $\overline{v_\phi^2} = v_{rot}^2 + \sigma^2$, and the last term in the previous equation vanishes. Using

$$\frac{\partial \Phi}{\partial R} = \frac{v_{circ}^2}{R} \quad (z=0), \quad (15)$$

one gets

$$v_{circ}^2 = v_{rot}^2 - \sigma^2 \left(\frac{\partial \ln \rho}{\partial \ln R} + \frac{\partial \ln \sigma^2}{\partial \ln R} \right), \quad (16)$$

where σ is the isotropic stellar velocity dispersion, v_{rot} the (observed) rotational stellar velocity, and v_{circ} the circular velocity in the $z=0$ plane in the potential corresponding to the density distribution $\rho(R, z)$. This equation is formally identically to that obtained from the Jeans equation in spherical symmetry, but is only valid in the $z=0$ plane.

In this plane, using the density distribution of a Hernquist sphere (Hernquist, 1990, corresponding to $\gamma=1$)

$$\rho(r) = \frac{Ma}{2\pi r} \frac{1}{(r+\alpha)^3} \quad (17)$$

we obtain

$$v_{circ}^2 = v_{rot}^2 + \left(4 - \frac{3\alpha}{R+\alpha} \right) \sigma^2, \quad (18)$$

neglecting the gradient of σ^2 compared to the gradient of the density. The coefficient of σ^2 in this equation goes to 1 for $R \rightarrow 0$ and to $5/2$ for $R \rightarrow \alpha$.

The right hand side of Equ. (18) is obtained from observational quantities of the stellar velocity field. We take the mean stellar rotation curve from Sect. 3.7 and deproject it using the optimal inclination of $i=30^\circ$. We assume σ to be isotropic and spherically symmetric (no deprojection) and calculate the mean velocity dispersion curve from the 4 independent stellar spectrograms (Fig. 6). The corresponding values of v_{circ}^2 in Eq. 18 are shown in Fig. 14 as circles. These are compared with the circular velocity curve from the axially symmetric part of the mass model (solid line in Fig. 14). Since the M/L ratio is a free parameter here, the amplitude of the circular velocity curve was adjusted to the observed points. The important conclusion here is that observed points and the circular velocity have the same radial profile; the stellar kinematics confirm our mass model.

For comparison we plot in Fig. 14b the inclination-corrected mean stellar rotation curve (+ symbols). This curve obviously has a shallower gradient and a lower peak rotational velocity, since it does not take into account the kinetic energy in σ . We also plot the inclination corrected ($i=30^\circ$) gas rotation curve at $P.A. = 118^\circ$ (triangles), which is near to the line-of-nodes (113°). The maximum gas rotation velocity reflects the mass model fairly well. We see that the gas rotates faster than the stars, as expected; however, the central gradient is again significantly shallower than that of the circular velocity curve.

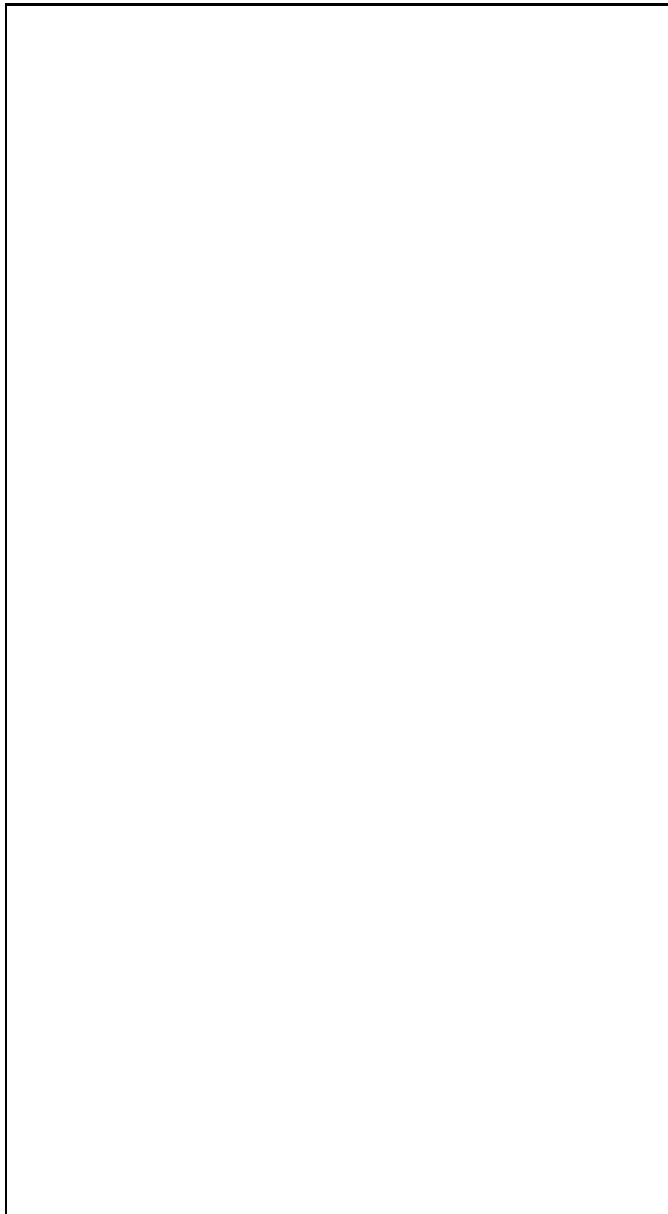


Fig. 14. a): The circular velocity, as calculated from the observed stellar rotation and velocity distribution by the Jeans equation (circles), agrees well with the the circular velocity derived from the mass model in Sect. 5.1 (solid and dotted curve, resp.). **b):** Same as above, plus the stellar rotation curve (+ symbols) and the gas velocity (triangles).

5.6. Kinematics of the gas

The mass model of Sect. 5.1 was used to study the dynamics of the optical line emitting gas. We neglect the self-gravity of this gas and consider it as test particles in the stellar potential.

Gas has a high cross-section, so encounters between gas clouds normally have to be taken into account. These encounters lead to dissipation of energy and angular momentum. As a first approximation we assume that the gas

clouds move on stable non-intersecting closed orbits (Sellwood & Wilkinson, 1993).

Figure 15 shows the stable closed orbits in our model (inside CR only prograde orbits are drawn). The orbits are shown in the corotating frame of reference. All orbit integrations were done using a 4th order Runge-Kutta integrator with variable time step and error prediction. This was mainly taken from *Numerical Recipes in C* (Press et al. 1992).

In the very center of Figure 15 one member of the x_2 -family is plotted, which shows the small extent of this orbit family. The ILR is at $5''$ which is small compared to the scale of the bar ($20''$) and that of the figure. The x_1 -orbits are highly elongated along the bar and become nearly round near the CR. Between the CR and the OLR there exist no non-intersecting orbits, so gas is swept out of this zone and piles up at the OLR. Beyond the OLR there exist again non-intersecting closed orbits that can be populated with gas. These orbits are nearly round but slightly elongated along the bar.

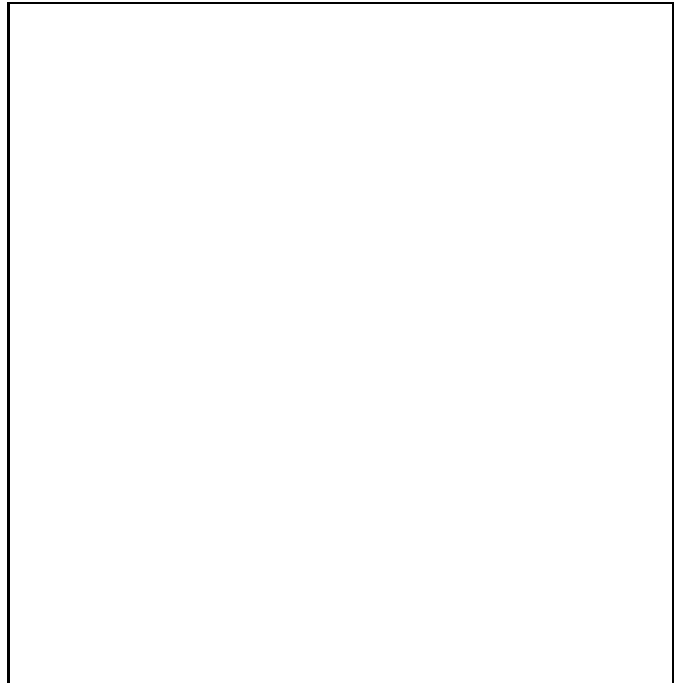


Fig. 15. Families of closed orbits in our model of M94. Resonances are marked on the lower margin. While the center is populated by x_1 - and x_2 -orbits, in the region between CR and OLR no stable nonintersecting orbits can be found. Beyond OLR there exist nearly round retrograde orbits (in the corotating frame) which make up the ring.

To obtain observable quantities from the orbits in Figure 15, one has to transform their velocities from the corotating frame to inertial coordinates and then project the orbits onto the sky. From the resulting velocity field we

calculate rotation curves at various position angles. Here we have to take into account that the velocity field is smoothed by atmospheric seeing ($1.5''$ FWHM), by the finite resolution of the spectrograph (120 km/sec FWHM), and by the finite slit width ($4.3''$). Therefore the gas velocity field has to be folded with the observed gas distribution in the region of the galaxy contributing to the corresponding slit position. To obtain a model of the gas distribution, we consider an E-W cut of the H_α distribution (Fig. 4), this is shown in Fig. 16. We approximate the central emission peak by an axially symmetric distribution with a radial profile $\sim (r + 2'')^{-1}$, and the ring at radius $r = 38''$ by a Gaussian profile ($8''$ FWHM).

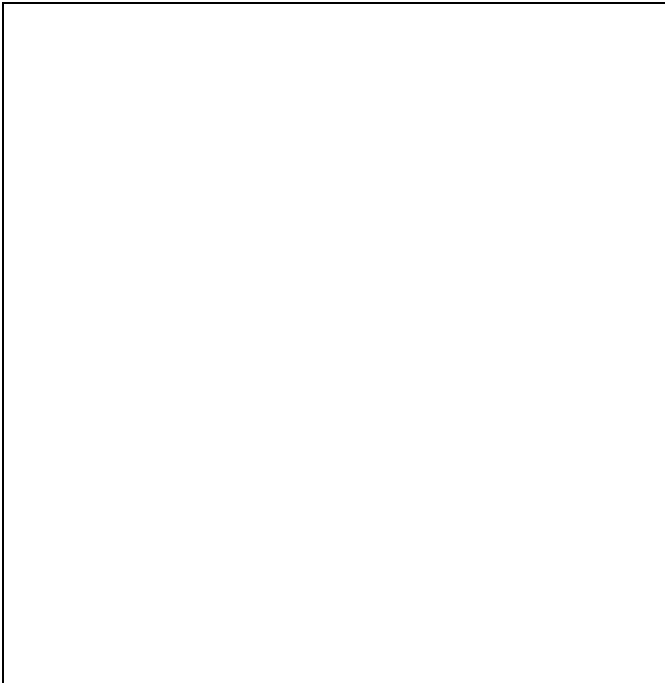


Fig. 16. Emission gas density along a cut through the center of M 94. Three peaks in the gas density are visible. The inner peak corresponds to the center of the galaxy, while the outer ones at $45''$ are due to the star forming ring, which is shown in Fig. 4. The resonances in our model are marked on the lower margin.

Two example rotation curves were obtained by this procedure and are shown by the \times symbols in Fig. 17a,b. The circles are the observed gas velocities along the corresponding slit positions. The dotted curves give the minimum and maximum velocities which occur in the considered slit area before smoothing by seeing and finite resolution.

Fig. 17a shows the model rotation curves along $P.A. = 118^\circ$, i.e. orthogonal to the bar. At radii greater $\approx 20''$ the agreement is quite good. This is because the orbits are nearly round there, so the velocities of the orbits reach

the circular velocity, which was used to calculate the mass of the model. However, between $5''$ and $10''$ the model curve shows a strong overshooting which arises from the contribution of the x_1 orbits along the direction of their maximum streaming velocity. The observed rotation curve is less steep in the center and does not show such strong humps. This is similar for the adjacent slit orientations (c.f. Fig. 8).

Fig. 17b shows the model rotation curves along $P.A. = 28^\circ$, i.e. parallel to the bar. As could be expected the rotation curve along the bar is nearly flat since the bar axis is nearly perpendicular to the line of nodes. Our model does not show the observed humps at this slit position. However, the maximum and minimum velocities are rather high, since our broad slit always covers the innermost x_1 orbits in their entirety. The slit smoothing gives the displayed smooth curve, but this may depend on the precise distribution of gas that contributes to the observed velocities. So the discrepancy in Fig. 17b is not as serious as in Fig. 17a.

Thus our kinematical model is not able to reproduce the observed peculiarities of the gas rotation curves. From the model we expect humps in the curves especially along the minor axis of the bar (i.e. when the slit orientation is orthogonal to the bar) from the x_1 orbits, and no humps on the major axis (spectrograms along the bar). Such a pattern is not observed, rather the distribution of humps and dips follows more circular patterns (spiral arms, Fig. 9).

As Fig. 8 shows, the gas rotation velocities are somewhat higher than the stellar velocities, but resemble these much better than the curve in Fig. 17a. This is all the more surprising since in the inner $15''$ (the region of greatest discrepancy) the bulge is hot and the kinematics in agreement with the mass model (Fig. 14). This suggests that the H_α gas in the inner $15''$ is both disturbed and still coupled to the stars. Cold molecular gas might well follow the model velocity field more closely, but corresponding high resolution CO data unfortunately are not available.

Our kinematical model was constructed in such a way that the outer Lindblad resonance coincides with the gas ring at $r \approx 45''$. Fig. 18 shows the comparison of the observed gas velocity on the ring compared with our model calculations.

6. Discussion

6.1. NGC 4736 - oval and barred

The I image (Fig. 1) and the ellipse fits (Fig. 2) show a clear nuclear bar in M 94 (NGC 4736), with axis ratio ~ 0.3 and linear length $\sim 30''$. The nuclear bar is implicit in the NIR data of Shaw et al (1993) and was also mentioned by Kormendy (1993). The galaxy NGC 4736 is known as a prototypical oval disk galaxy. Such oval disks can be recognized both photometrically and kinematically

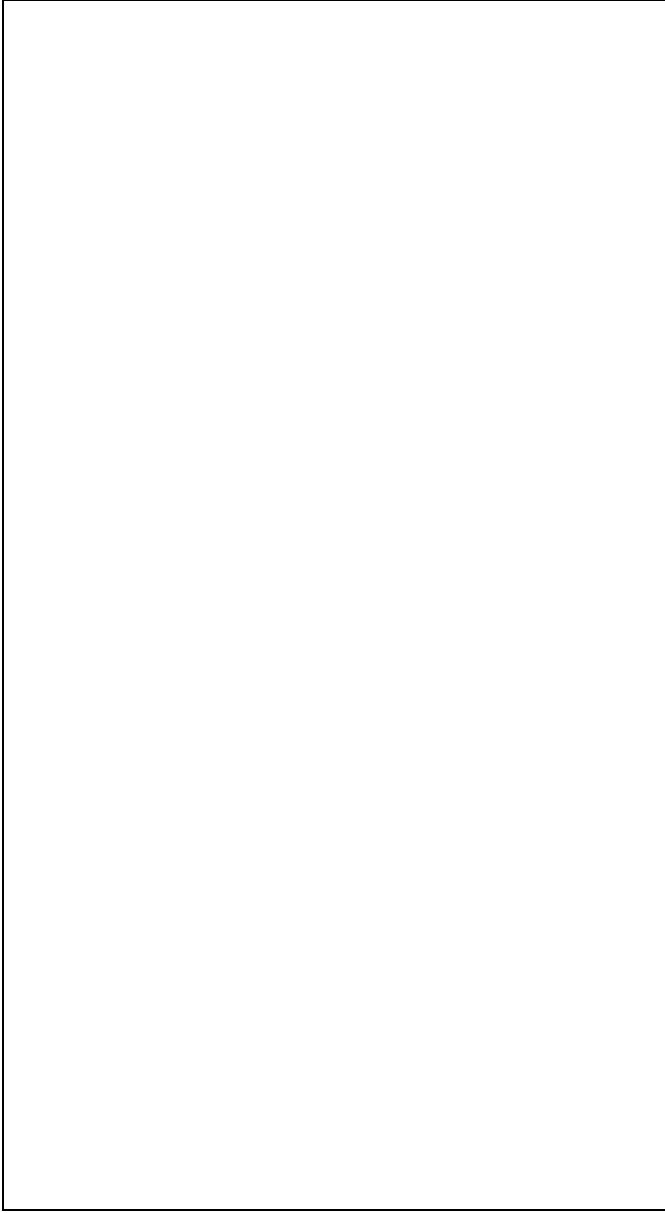


Fig. 17. Rotation curves along P.A. = 118° (top) and P.A. = 28° (bottom). The circles are the observed velocities, the crosses are the theoretical values. The dots give the minimal and maximal velocity in every seeing element. For radii greater than $\approx 20''$ the agreement is quite good. At the center the rise of the theoretical velocities is too steep to match the observations.

(Kormendy 1982). Photometrically the brightness distribution consists of a series of distinct regions, which each have elliptical isophotes and a noticeable outer edge. The axial ratios and position angles of the isophotes in these nested oval regions are different, implying that at most one of them can be axisymmetric if they are all coplanar. Kormendy (1982) argues that warps are rare in edge-on spirals at the high surface brightnesses at which the oval struc-

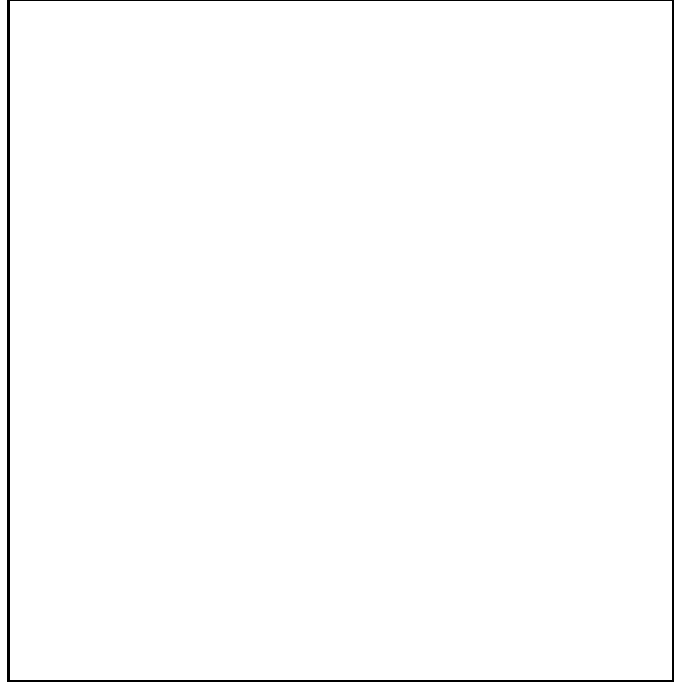


Fig. 18. Measured velocities of gas in the ring of M 94 with respect to the center, as a function of position angle. The asterisks represent our measurements in Sect. 3.8. The other symbols indicate different emission lines from van der Kruit (1974). The dotted lines give the theoretical predictions based on closed orbits in the ring with approximate radii of $42''$, $47''$ and $51''$.

tures occur ($< 25B\text{-mag arcsec}^{-2}$) and that therefore the observed features must be truly non-axisymmetric. Kinetically, oval disks signify their presence by several features in their velocity fields which are also known from barred or triaxial galaxies: The kinematic major axis is different from the photometric major axis, it is not perpendicular to the kinematic minor axis, and its position angle may change with radius. These signatures arise from the projection of quasi-elliptical stellar orbits or gaseous streamlines orientated at oblique angles with respect to the line-of-sight and line-of-nodes.

The B-band surface brightness profile of M 94 was measured by Boroson (1981); it appears to show several characteristic radii: $40''$ and $120''$. Our I, J, K brightness profiles confirm the shelves at $40''$ (1.3 kpc) and $120''$, although the feature at $40''$ is less pronounced. The reason for this is probably the blue color of the star forming ring at $r = 45''$. Numerous large HII regions are located on this inner ring which modify the blue surface brightness profile (Fig. 4). The inner ring is also seen in HI (at $40\text{--}50''$, Bosma et al 1977, Mulder & van Driel 1994), in CO (Garman & Young 1986, Gerin, Casoli & Combes 1991), and in $H\alpha$ (Fig. 4, van der Kruit 1974, Buta 1988). The outer disk of the galaxy is not obviously barred, but the run with radius of ellipticity and position angle suggests

an oval shape (Fig. 2). M94 is well known for its faint outer ring at $\sim 330''$ seen in *HI* and the stellar distribution (e.g. Plate I in Lindblad 1961 or Fig. 1b in Mulder & van Driel 1993). From our kinematic and photometric study we think it is most likely that the inclination of M94 is $i \approx 35^\circ$, so that the most axisymmetric region is that portion of the disk between $50''$ (1.7 kpc) and $100''$ (3.3 kpc, Sect. 3.3).

The kinematics of the *HI* and H_α gas at medium and large radii show significant departures from axial symmetry. A recent model of the outer oval disk is presented by Gerin et al (1991), who assume an oval shape of the potential between 5.5 kpc and 13 kpc and associate the two rings with the inner and outer Lindblad resonances (ILR and OLR) of this rotating oval. In Sect. 3.3 we concluded, that the disk of M94 is oval at least between $120''$ (4 kpc) and $220''$ (7.5 kpc); the inner radius is compatible to the values of Gerin et al, our outer value is lower. However, since the ellipticity of the disk still increases between 220 and $400''$, the oval disk might well be larger.

The modelling presented in this paper, based on optical CCD and NIR observations of the central bulge and bar, suggests that the most likely value for the pattern speed is such that the OLR of the bar coincides with the position of the inner *HI* and H_α ring at $45''$. Combining this result with the simulations of Gerin et al (1991) it thus appears that M94 is a galaxy with an inner bar embedded in an outer oval disk, such that the OLR of the inner component is located approximately at the ILR of the outer component. Such bar-within-oval galaxies share many of the characteristics of the bar-within-bar galaxies discussed, e.g., by Pfenniger & Norman (1990) and Friedli & Martinet (1993). In the following, we discuss some aspects of this picture for M94 in more detail.

6.2. Nuclear bulge and nuclear bar?

Does NGC 4736 have a nuclear bulge? On the basis of earlier photometry and kinematic measurements, Kormendy (1993) concluded that M94 is one of a class of galaxies that appear to contain central bulges which are really only disks. The evidence he presented in favour of this view was the following: (i) The central component with the $r^{1/4}$ brightness profile ('bulge') coincides spatially with spiral structure and a nuclear bar. These features are characteristic for disks; thus the $r^{1/4}$ profile cannot *per se* be used as evidence for a truly three-dimensional bulge. (ii) Based on data by Pellet & Simien (1982), the apparent $v/\sigma \simeq 0.77$ of NGC4736 is well above that expected for an oblate isotropic rotator of its flattening ($\epsilon \simeq 0.1$, $(v/\sigma)_{\text{obl}} \simeq 0.35$). Thus the central kinematics appear disk-like rather than bulge-like.

With the new data presented in this paper we can now investigate this question in more detail. The stellar velocity dispersion profile (Fig. 6) shows a clear transition from an outer cold disk to an inner hot component.

Because we are observing M94 nearly from above, the measured dispersion mostly characterizes the vertical motions in this galaxy. Outside $15''$ the observed dispersion is consistent with the instrumental resolution ($\sim 60 \text{ km s}^{-1}$) and at those radii the light may be dominated by a cold disk component. In this region the circular velocity is $v_c \sim 200 \text{ km s}^{-1}$. Inside $15''$, the projected velocity dispersion rises to 120 km s^{-1} , while simultaneously the measured rotation velocity linearly decreases inwards to zero.

From the (admittedly noisy) line-of-sight-velocity distribution ('LOSVD') shown in Fig. 7, we see that in fact the rotation velocity at $10''$ is still dominated by the narrow peak corresponding to the rapidly rotating disk. However, the bulge has a much broader, more symmetric LOSVD with a mean rotation velocity of $\simeq 50 \text{ km s}^{-1}$. This value reduces the *intrinsic bulge* V_{max}/σ to a value of ~ 0.8 (deprojected), which is more in accord with its *intrinsic* flattening of $q \approx 0.6$ (deprojected with $\epsilon = 0.1$ and $i = 35^\circ$).

If indeed the entire central light came from a constant-thickness disk, then the observed surface brightness profile, which is consistent with a projected Hernquist model, would imply a surface brightness $\propto R^{-1}$, and hence a vertical velocity dispersion $\propto R^{-1/2}$. Given our limited resolution, the predicted rise in the vertical dispersion by a factor ~ 2 between $15''$ and $3''$ is consistent with the measured value of the central dispersion. However, the shape of the velocity dispersion profile, in particular the clear decay at around $15''$, argues in favour of a three-dimensional central bulge component, supporting the analysis of the LOSVD above.

We next discuss the nature of the central bar. From the photometry we infer that the bar comprises only $\sim 15\%$ of the light within $20''$. The light distribution is significantly more axisymmetric in the region $r < 10''$ and $r > 20''$ than near $r = 15''$ where the bar is strongest in the surface brightness profile (Fig. 2). The new surface photometry shows that the bar signature disappears very quickly for $r > 15''$. The brightness distribution cannot be fitted with a single ellipsoidal component as the isophotes are far too pointed near the end of the bar (a_4 profile in Fig. 2). A strong gradient in the ellipticity and boxyness parameter a_4 would be required in a one-component model. This rules out a single triaxial bulge with nearly constant axis ratio as an explanation of the data. However, it also argues against a single disk-like component, for this would have to be almost completely axisymmetric in the inner $10''$ and develop a separate thin ($b/a \sim 0.3$) bar component near $r = 15''$, a morphology which is not usually seen in bulge-less, barred galaxies.

Because the projected length of the bar ($15''$), the size of the bulge, and the scale of the linearly rising part of the rotation curve (Fig. 6) all coincide, we can not use the velocity dispersion data to determine the vertical extent of the bar. Indeed, the fact that these scales approximately agree might suggest that the bar and the bulge could after

all be one and the same component. However, the brightness profile of the bar is much shallower than that of the bulge, so that in this interpretation the quadrupole component would have to be strongly concentrated towards the outer parts of the bulge. Moreover, along its minor axis direction, the bar is significantly smaller ($\approx 7''$) than the bulge ($15''$). The former property appears consistent with the properties of peanut/box-shaped bulges, which – compared to an ellipsoidal model – have more excess flux near their edges than in their central parts (Shaw 1993). The latter property can not be compared with these objects because peanut bulges are usually observed edge-on.

Taken together, the photometry and stellar kinematics of M 94 therefore appear to show that this galaxy contains a small central bulge, a centrally concentrated disk, and a weak $30''$ diameter bar with shallower profile than either of the former two components. The bulge may be superposed on the central disk and bar, or, perhaps more likely, because of the similar surface brightness profiles of bulge and disk, simply be the inner, more spherical part of the disk.

6.3. Pattern speed of the central bar

The model discussed in the previous Section assumed that the bar rotates at a pattern speed $\Omega_p = 290 \text{ km s}^{-1} / \text{kpc}$, such that corotation lies at $25''$. This places the inner ring of $H\text{I}$ and H_α gas at approximately the OLR of the rotating potential; as shown by Schwarz (1981) gas between CR and OLR is given angular momentum by the bar, moves outwards and collects in a ring of material near the OLR. This zone interior to the OLR is characterized by a weak spiral pattern, which can best be seen in the morphology of the dust lanes (Fig. 5). The corotation radius then corresponds approximately to the end of the bar in the CCD image (Fig. 1 and Fig. 10), and to the region of lowered cold gas density visible in the CO observations of Gerin et al (1991). The depression near corotation is extremely pronounced in the H_α emission distribution (Fig. 4 and Fig. 16).

Although a model with this value of Ω_p thus explains a number of features observed in M 94, it failed in the sense that the measured H_α gas kinematics in the central $15''$ are not fitted by those predicted if the gas moved on closed orbit streamlines in the barred potential. However, this may be more a problem to do with the H_α gas: indeed for no reasonable value of the pattern speed was it possible to obtain a satisfactory fit to the H_α kinematics. In any case it is unlikely that the bar could rotate faster, for then corotation would be placed inside the bar. There would be no orbits to support the outer bar, yet the stellar population of the bar appears old ($\gtrsim 3 \text{ Gyr}$).

Could the bar rotate more slowly? This at least would go in the sense of somewhat easing the discrepancy of the predicted and the H_α kinematics. In this case the inner ring at $45''$ might be at ILR rather than at OLR, and

then the bar's pattern speed would be equal to the pattern speed of the outer oval in the Gerin et al model. If this were the case, the bar would end inside its ILR. However, such a model could only be in dynamical equilibrium if the principal axes of bar and oval were either aligned or perpendicular to each other (Louis & Gerhard 1988), neither of which possibility is in accord with the observed misalignment angle between bar and adjacent disk: From $P.A._{bar} = 28^\circ$ and $P.A._{oval} = 90^\circ$ we get $\Delta \approx 62^\circ$ in the sky or $\sim 58.5^\circ$ in the plane of the galaxy for $i = 35^\circ$. If, on the other hand, the two components are oriented at an oblique angle, then torques between them will have a strong effect particularly for low pattern speeds. Thus we conclude that the value of $\Omega_p = 290 \text{ km s}^{-1} / \text{kpc}$ that we have used is the most likely one.

Models with two non-axisymmetric components rotating at different pattern speeds were discussed and generated by Pfenniger & Norman (1990) and Friedli & Martinet (1993). These authors concluded that in order to avoid too large resonant and chaotic zones in the orbit distribution it was favourable to place the ILR of the outer, more slowly rotating component onto the CR resonance of the inner, more rapidly rotating bar. Indeed, in the numerical (N-body and SPH) simulations of Friedli & Martinet (1993) two-bar systems with the corresponding ratio of pattern speeds formed. In the formation of the inner secondary bar, dissipation is found to be critical in assembling sufficient amounts of gas onto the x_2 -orbits in the primary bar potential.

However, the two-bar phase in these models only lasts for about five rotations of the faster, inner bar, after which this dissolves. Therefore, if this is to be a viable scenario for M 94, the inner bar must have been triggered very recently, e.g., by infalling molecular gas, and it must currently end somewhat outside its ILR. This appears difficult in the dominant field of a nearly axisymmetric component. Moreover, the stars themselves in the M 94 bar are several times older than the estimated dissolution timescale. Thus one would require that during their bar triggering no young stars, formed in the molecular clouds, should have been mixed into the stellar bar, which appears unlikely. Alternatively, if the inner bar indeed rotated faster, such that the ring is at OLR, then the interaction with the outer oval would be weaker because of the adiabatic invariants, and the lifetime of this configuration could be longer.

6.4. Dynamics of the inner H_α -emitting gas

Warm optical emission gas can be detected in M 94 mainly in the inner star forming ring ($r \approx 45''$) and in the central bar region. The dynamics of the ring was studied in detail by van der Kruit (1974, 1976) and Buta (1988). The velocity field of the innermost region is fairly complex. There are several aspects:

(1) The H_α streaming velocities measured in the central $15''$ of M 94 are very similar to the stellar streaming velocities in the bulge (Fig. 8). These correspond to a hot stellar system, as the deprojected rotation is $v^2 \simeq \sigma^2/2$ at $10''$ (Sect. 5.5). Thus the H_α streaming velocities are significantly less than the circular velocity estimated from the Jeans equation. However, the gas rotates faster than the stars for $r > 20''$, fitting to the HI rotation curves of Mulder & van Driel (1993).

(2) The gas velocity field does not reflect the high streaming velocities expected from closed orbit streamlines in the barred potential. In particular, the expected steep rise of the measured velocities in the central $5''$ for slit positions orthogonal to the bar is not reproduced.

(3) The warm gas velocity field shows, superposed on the general near-circular rotation field, a number of humps and dips which seem to correlate with the weak dust spiral pattern observed in the region between central bar and ring (Fig. 9).

We now discuss several possible explanations for the observed low gas velocities in the very center.

(a) The gas velocities are intrinsically higher, but we do not observe the high values because of low spatial resolution (seeing and broad slit) combined with the finite spectral resolution. These effects were taken into account for the construction of the rotation curves in Fig. 17, so this possibility can be rejected.

(b) The gas in the region of the central bar moves intrinsically similar as the stars. This might be plausible if the observed gas originated from mass loss from the old stars, and still shared their velocity field.

(c) Walker et al (1988) published $2.0 - 2.5\mu m$ spectra from the central $8''$ region of M 94. They showed that the B_γ emission is very weak there compared to typical starburst galaxies like M 82 or NGC 253. Therefore no strong star formation is presently going on in the center, consistent with the not very strong H_α emission from the central region. However, from the still relative strong CO absorption bands of young supergiants Walker et al (1988) concluded that a strong starburst did occur in the central region of M 94 some 10^7 years ago. A burst of star formation produces wind bubbles and supernova shocks unrelated to the potential of the galaxy. Presently, the nuclear region of M 94 contains a mixture of warm gas, warm dust, and molecular clouds (Smith et al 1991). The warm gas might not yet have settled to cloud orbits in the plane, making its present partly chaotic velocity field plausible.

It will be interesting to compare future high-resolution molecular gas kinematics with the model streamlines in Sect. 5.

7. Conclusions

(1) We have reported CCD imaging in I and H_α , focal reducer imaging in V , I , and NIR J , K imaging of the bright Sab galaxy M 94 (NGC 4736). This galaxy is known as

an oval disk galaxy. Two rings, an outer ring observed at $330''$ and an inner ring at $45''$, are thought to be located near the outer and inner Lindblad resonances (OLR and ILR) of this rotating oval (Gerin et al 1991). Our study of the surface brightness profiles and isophote shapes confirms the oval disk structure of M 94 between $r = 120''$ and $r = 220''$. Basic parameters of M 94 and the most important numerical results from our work are collected in Table 1.

(2) The central surface brightness distribution of M 94 is characterized by a power-law profile. It is not possible to discriminate bulge and disk components from the photometry alone. We have constructed a morphological model of the inner regions in terms of an axisymmetric model with a $\gamma = 0.9$ cusp and scale-length $\alpha = 15''$ (Dehnen & Gerhard 1994). Outside $r = 60''$ a nearly exponential disk with scale-length $\beta \approx 60''$ must be added to this model.

(3) Inside the inner ring the position angles of the isophotes rotate by nearly 90° . The isophotes show cusped deviations from ellipses in a range of radii just interior to $r = 15''$. After subtracting the axisymmetric model, the residuals show a nuclear bar, with projected radius $r = 15''$, axial ratio $b/a = 0.3$ and $P.A. = 28^\circ$. The outer oval disk has $P.A. = 90^\circ$; the deprojected misalignment angle between these two components in the plane of the galaxy is $\Delta = 58.5^\circ$. The luminosity of the inner bar is $5.9 \cdot 10^8 L_\odot$ (in B), comprising about 14% of the total light inside $20''$.

(4) Thus M 94 has a bar-within-bar morphology. We suggest that the corotation radius of the inner bar is just outside its deprojected major axis length ($20'' = 0.64$ kpc). This places the inner gas ring (at $45''$), which is believed to fall near the ILR of the outer oval, at the OLR of the central bar. The zone near corotation (CR at $26''$) is characterized by a marked depression in the H_α and HI gas densities, consistent with the absence of non-intersecting closed orbits in this region. Between CR and OLR of the central bar, spiral arms are detectable, especially well by their thin dust lanes in, e.g., $I - K$ color index images.

(5) We have presented absorption line spectroscopy in 4 longslit orientations in the inner $60''$ of M 94. The stellar velocity dispersion profile reveals the existence of a central bulge of $15''$ radius, with $\sigma = 120 \text{ km s}^{-1}$. Outside the bulge we observe $\sigma = 60 \text{ km s}^{-1}$ in the disk region, which is the spectral resolution. The stellar rotation curves are smooth and are consistent with an axially symmetric velocity field with inclination $i = 30^\circ$ and a line of nodes at $P.A. = 113^\circ$. This suggests that the effects of the nuclear bar on the stellar velocity field are weak, in the bulge region because this is a hot stellar system, and outside the bar because there the potential becomes rapidly axisymmetric. The combination of stellar rotation and velocity dispersion is consistent with the photometric model in the bulge and adjacent disk regions in the sense that the Jeans equation is satisfied for $M/L_B \approx 1.8$.

(6) Further evidence that the bulge and disk components in M 94 are distinct comes from the line-of-sight velocity profiles at positions along the minor axis but beyond the extent of the nuclear bar, which suggest a rapidly rotating, cold component superposed onto a more slowly rotating, hot component. From these profiles we estimate that the deprojected mean rotation of the bulge is $v \approx 100 \text{ km s}^{-1}$, and that $v/\sigma = 0.8$, roughly consistent with an intrinsic bulge axis ratio $c/a = 0.6$.

(7) By contrast, the kinematic data do not allow us to determine whether the bulge and bar components are distinct. The result that the radius of the bulge and the major axis length of the bar are similar might suggest that, in fact, bulge and bar are one and the same component, perhaps similar to that inferred in the inner Galaxy. However, the bar is significantly smaller along its minor axis direction than the bulge, so that a simple near-ellipsoidal component is not a good model for the data.

(8) We have obtained emission line spectroscopy in 8 longslit orientations of the inner $100''$ of M 94, and thus obtained new results on the gas kinematics in the region of the inner bar. The streaming velocity field of the 10^4 K gas is similar to that of the stars for $r < 20''$. The gas rotates faster than the stars and fits the HI rotation field (Mulder and van Driel 1993) at larger radii, consistent with circular orbits.

(9) Orbit calculations in the gravitational potential derived from the photometry of M 94 predict large non-circular motions for cold gas in equilibrium in the bulge region. The resulting kinematics do not reproduce the observed central H_α kinematics. For the future it would be extremely interesting to compare high-resolution CO gas velocity observations with the model predictions.

(10) The result that the H_α streaming velocities in the inner $15''$ are less than required for gravitational equilibrium suggests that the warm ionized gas has significant random motions. This could be because this gas is still associated with the stars through recent mass loss, or, perhaps more likely, that it is being heated by shocks and localized gas flows. Indeed, while Walker et al (1988) found no B_γ in the central $8''$ in M 94, i.e. no signs for an on-going starburst, they concluded from the strengths of the CO bands that a strong starburst must have occurred several 10^7 yr ago. Direct evidence for some still ongoing star formation in the inner regions of M 94 also comes from the observed H_α emission.

Acknowledgements. We thank the Calar Alto observatory staff for the support during the observations. We thank the MAGIC crew (Heidelberg) for the efficient support during the NIR campaign. We thank C. Scorca (Heidelberg) and P. Surma (Cambridge) for the exposure of the focal reducer images and F. Baier and H. Tiersch (Potsdam) for the exposure of the H_α image. We are grateful to R. Kohring (Heidelberg) for substantial support during the reduction of the emission line spectrograms. We acknowledge the use of the Fourier-cross-correlation routine of R. Bender (München) and the γ -routine of W. Dehnen

(Oxford). The SIMBAD data base in Strasbourg was used to search for references of M 94. This work was supported by the *Deutsche Forschungsgemeinschaft* via the *Sonderforschungsbereich 328*.

References

- Bender, R.: 1990, *Astron. Astrophys.* **229**,441
 Bender, R., Möllenhoff, C.: 1987, *Astron. Astrophys.* **177**,71
 Beckman, J.E., Varela, A.Q.M., Muñoz-Tuñón, C., Vilchez, J.M., Cepa, J.: 1991, *Astron. Astrophys.* **245**,436
 Binney, J, Tremaine, S.: 1987, *Galactic Dynamics*, Princeton University Press, 1.edition
 Boroson, T.: 1981, *Astrophys. J. Suppl. Series* **46**,177
 Bosma, A., van der Hulst, J.M., Sullivan, III, W.T.: 1977, *Astron. Astrophys.* **57**,373
 Buta, R.: 1984, *The Structure and Dynamics of Ringed Galaxies*, Ph. D. Thesis, University of Texas, Austin
 Bronstein, I.N., Semendjajew, K.A : 1987, *Taschenbuch der Mathematik*, Teubner, Leipzig
 Buta, R.: 1988, *Astrophys. J. Suppl. Series* **66**,233
 Contopoulos, G., Grosbøl, P.: 1989, *Astron. Astrophys. Rev.* **1**,261
 Dehnen, W.: 1993, *Monthly Notices Roy. Astron. Soc.* **265**,250
 Dehnen, W., Gerhard, O.E.: 1994, *Monthly Notices Roy. Astron. Soc.* **268**,1019
 de Vaucouleurs, A., Longo, G.: 1988, *Catalogue of Visual and Infrared Photometry of Galaxies from 0.5 μm to 10 μm (1961 - 1985)*, Univ. of Texas Monographs in Astron. No. 5, Austin, 1988
 Duric, N., Dittmar, M.R.: 1988, *Astrophys. J. Letters* , **332**,L67
 Ferrers, N.M.: 1877, *Quart. J. Pure Appl. Math.* **14**:1,1877
 Friedli, D., Martinet, L.: 1993 *Astron. Astrophys.* , **277**,27
 Garman, L.E., Young, S.J.: 1986, *Astron. Astrophys.* , **154**,8
 Gerin, M., Casoli, F., Combes, F.: 1991, *Astron. Astrophys.* **251**,32
 Herbst, T.M., Beckwith, S.V.W., Birk, C., Hippler, S., McCaughrean, M.J., Manucci, F., Wolf, J.: 1993, 'Infrared Detectors and Instrumentation', Conference 1946, SPIE, p.605
 Hernquist, L.: 1990, *Astrophys. J.* **356**,359
 Kormendy, J.: 1982, in *Morphology and Dynamics of Galaxies*, L. Martinet, M. Mayor (eds.), Geneva Obs., Sauverny, P. 113
 Kormendy, J.: 1993, in *IAU Symposium 153, Galactic Bulges*, H. Habing, H. Dejonghe (eds.), Dordrecht, p. 209
 Keel, W.C., Weedman, D.W.: 1978, *Astron. J.* , **83**,1
 Lindblad, P.O.: 1960, *Stockholms Obs. Annaler* **21**, No.4
 Louis, P.L., Gerhard, O.E.: 1988, *Monthly Notices Roy. Astron. Soc.* **233**,337
 Matthias, M.: 1993, Diploma thesis, University of Heidelberg
 Mulder, P.S., van Driel W.: 1993, *Astron. Astrophys.* **272**,63
 Pellet, A., Simien, F.: 1982, *Astron. Astrophys.* **106**,214
 Pfenninger, D., Norman, C.: 1990, *Astrophys. J.* **363**,391
 Pogge, R.W.: 1989, *Astrophys. J. Suppl. Series* **71**,433
 Press, W.H., Flannery, B.P., Teukolsky, S.A., Vetterling, W.T.: 1992, *Numerical Recipes, C-Version*, Cambridge Univ. Press, Cambridge, 1992
 Schwarz, M.P.: 1981, *Astrophys. J.* **247**,77
 Sellwood, J.A., Wilkinson, A.: 1993, *Reports on Progress in Physics* **56**, No.2, 173
 Shaw, M.: 1993, *Monthly Notices Roy. Astron. Soc.* **261**,718

- Shaw, M.A., Combes, F., Axon, D.J., Wright, G.S.: 1993, *Astron. Astrophys.* **273**,31
- Shlosman, I., Frank, J., Begelman, M.C.: 1989, *Nature* **338**,45
- Smith, B.J., Lester, D.F., Harvey, P.M., Pogge, P.W.: 1991, *Astrophys. J.* **373**,66
- Tohline, J.E., Simonson, G.F., Caldwell, N.: 1982, *Astrophys. J.* **252**,92
- van der Kruit P.C.: 1974, *Astrophys. J.* **188**,3
- van der Kruit P.C.: 1976, *Astron. Astrophys.* **52**,85
- Walker, C.E., Lebofsky, M.J., Rieke, G.H.: 1988, *Astrophys. J.* **325**,687

Table 1. Parameters of M94

	Item	Quantity	Reference
General Parameters	type	(R)Sab(s) resp. (R)SA(r)ab II	RSA resp. RC2
	distance	6.6 Mpc	
	scale	$1'' = 32pc$	
	v_{sys}	310 km/s	Buta 1988
	mass	$5.1 \times 10^{10} M_{\odot}$	Mulder & van Driel 1993
	B_t	8.96 mag	Buta 1988
Morphology on Sky	bulge	$r = 15 - 20''$	Sect. 3.7
	central bar	$a = 15'', b = 7'', P.A. = 28^{\circ}$	Sect. 3.1
	inner ring	$r = 45'', P.A. = 127^{\circ}, \varepsilon = 0.27$	van der Kruit 1976
	oval disk	$r = 120 - 220'', P.A. \approx 95^{\circ}, \varepsilon = 0.23$	Sect. 3.2
	outer ring	$r \approx 330'', P.A. \approx 150^{\circ}$	Buta 1988
Inner Disk+Bulge Surface Photometry	brightness profile	$\gamma = 0.9, \alpha = 15''$	Sect. 3.2
	ellipticity	$\varepsilon \approx 0.18$	Sect. 3.4
	position angle	$P.A. \approx 110^{\circ}$	Sect. 3.4
	inclination	$i \approx 35^{\circ}$	Sect. 3.4
	mass of inner disk	$7.0 \times 10^9 M_{\odot}$	Sect. 5.1
Bulge Model	flattening	$q = 0.4$	Sect. 3.7
	mass	$2.0 \times 10^9 M_{\odot}$	Sect. 5.1
	v/σ	0.8	Sect. 3.7
	M/L_B	1.8	Sect. 5.1
Central Bar Model	axis lengths (deprojected)	$a = 21'', b = 7''$	Sect. 5.1
	mass	$9.8 \times 10^8 M_{\odot}$	Sect. 5.1
	pattern speed	290 km/s/kpc	Sect. 5.4
	ILR inner Lindblad res.	$5'' \hat{=} 160pc$	Sect. 5.4
	CR corotation radius	$26'' \hat{=} 830pc$	Sect. 5.4
	OLR outer Lindblad res.	$40'' \hat{=} 1280pc$	Sect. 5.4
Stellar Kinematics	v_{rot} (deprojected)	230km/sec max. at $15''$	Sect. 5.2
	velocity dispersion	120 km/sec	Sect. 3.7
	inclination	$i = 30^{\circ}$	Sect. 3.7
	line of nodes	$P.A. = 113^{\circ}$	Sect. 3.7
Gas Kinematics	v_{rot} (deprojected)	250km/sec max. at 15-20''	Sect. 3.8
HI	mass	$10^9 M_{\odot}$	Mulder & van Driel, 1993
	v_{rot}	130 – 170km/s	Mulder & van Driel, 1993
	inclination	$i \approx 40^{\circ}$	Mulder & van Driel, 1993
	line of nodes	$P.A. \approx 115^{\circ}$	Mulder & van Driel, 1993
Molecular Gas	H_2 mass	$5.1 \times 10^8 M_{\odot}$	Gerin et al 1991
	v_{rot}	200 km/s at $60''$	Gerin et al 1991